Comparative proximity biotinylation implicates RAB18 in cholesterol mobilization and biosynthesis — Source link ↗

Robert S. Kiss, Chicoine J, Khalil Y, Robert Sladek ...+13 more authors

Institutions: McGill University, University College London, University of Leeds, University of Oxford ...+1 more institutions

Topics: Biotinylation, EMOPAMIL-BINDING PROTEIN and Nucleotide exchange factor

Related papers:

- Rab18 and a Rab18 GEF complex are required for normal ER structure

- RabGEFs are a major determinant for specific Rab membrane targeting.

- Toward a comprehensive map of the effectors of rab GTPases.

- Large Scale Screening for Novel Rab Effectors Reveals Unexpected Broad Rab Binding Specificity

- A conserved and regulated mechanism drives endosomal Rab transition

Share this paper: ⓕ 🐦 in ✉

1   TITLE

2   Comparative proximity biotinylation implicates RAB18 in cholesterol mobilization and

3   biosynthesis

4

5   RUNNING TITLE

6   GEF-dependent RAB18 interactions

7

8   AUTHORS

9   Robert S. Kiss*[1], Jarred Chicoine[1], Youssef Khalil[2], Robert Sladek[1], He Chen[1],

10   Alessandro Pisaturo[1], Cyril Martin[1], Jessica D. Dale[3], Tegan A. Brudenell[3], Archith

11   Kamath[4,5], Emanuele Paci[6], Peter Clayton[2], Jimi C. Wills[4], Alex von Kriegsheim[4],

12   Tommy Nilsson[1], Eamonn Sheridan[3], Mark T. Handley*[3,7]

13

14   AFFILIATIONS

15   [1]Research Institute of the McGill University Health Centre

16   1001 boul Decarie

17   Glen Site Block E

18   Montreal, QC

19   H4A 3J1

20   Canada

21

22   [2] Genetics and Genomic Medicine

23   Great Ormond Street Institute of Child Health

24   University College London

25   30 Guilford Street

26   London

27   WC1N 1EH

28   United Kingdom

29

30   [3]Leeds Institute of Medical Research

31   St James's University Hospital

32   Leeds

33   LS9 7TF

34   United Kingdom

35

36   [4]Cancer Research UK Edinburgh Centre

37   MRC Institute of Genetics & Molecular Medicine

38   The University of Edinburgh

39   Western General Hospital

40   Edinburgh

41   EH4 2XR

42   United Kingdom

43

44   [5]Medical Sciences Division

45   University of Oxford

46   Oxford

47   OX3 9DU

48   United Kingdom

49

50   [6]Astbury Centre for Structural Molecular Biology

51   University of Leeds

52   Leeds

53   LS2 9JT

54   United Kingdom

55

56   [7]Faculty of Biological Sciences

57   University of Leeds

58   Leeds

59   LS2 9JT

60   United Kingdom.

61

62   *authors contributed equally

63

64   CORRESPONDING AUTHORS

65   Robert S. Kiss: robert.kiss@mcgill.ca

66   Mark T. Handley: m.handley@leeds.ac.uk

67

68   KEYWORDS

69   RAB18, BioID, Cholesterol, Lathosterol, EBP, ORP2

70

71   SUMMARY STATEMENT

72   We used proximity biotinylation together with guanine nucleotide exchange factor

73   (GEF)-null cell lines to discriminate functional RAB18-interactions. Our data suggest

74   that RAB18 mediates lathosterol mobilization and cholesterol biosynthesis.

75

76   ABSTRACT

77   Loss of functional RAB18 causes the autosomal recessive condition Warburg Micro

78   syndrome. To better understand this disease, we used proximity biotinylation to

79   generate an inventory of potential RAB18 effectors. A restricted set of 25 RAB18-

80   interactions were dependent on the binary RAB3GAP1-RAB3GAP2 RAB18-guanine

81   nucleotide exchange factor (GEF) complex. Consistent with a role for RAB18 in

82   regulating membrane contact sites (MCSs), interactors included groups of

83   microtubule/membrane-remodelling proteins, membrane-tethering and docking

84   proteins, and lipid-modifying/transporting proteins. We provide evidence validating

85   novel interactions with SEC22A and TMCO4. We also provide functional evidence

86   that RAB18 links the Δ8-Δ7 sterol isomerase emopamil binding protein (EBP) to a

87   molecular machinery mobilizing the products of EBP-catalysis. The cholesterol

88   precursor lathosterol accumulates in RAB18-null cells, and *de novo* cholesterol

89   biosynthesis is reduced. Our data demonstrate that GEF-dependent Rab-interactions

90   are highly amenable to interrogation by proximity biotinylation and suggest that Micro

91   syndrome is a cholesterol biosynthesis disorder.

92

5

93 INTRODUCTION

94 Rab Proteins are a large subfamily of small GTPases with discrete roles in

95 coordinating membrane trafficking (Zhen & Stenmark, 2015). Like other small

96 GTPases, they adopt different conformations and enter into different protein-protein

97 interactions according to whether they are GDP-, or GTP-bound. Although they

98 possess some intrinsic GTP-hydrolysis activity, their *in vivo* nucleotide-bound state is

99 tightly governed in cells by two classes of regulatory proteins. Guanine-nucleotide

100 exchange factors (GEFs) catalyse the exchange of bound GDP for GTP while

101 GTPase-activating proteins (GAPs) promote the hydrolysis of bound GTP to GDP

102 (Barr & Lambright, 2010, Lamber et al., 2019).

103 Biallelic loss-of-function variants in *RAB18*, *RAB3GAP1*, *RAB3GAP2*, or *TBC1D20*,

104 cause the autosomal recessive condition Warburg Micro syndrome (Aligianis et al.,

105 2005, Bem et al., 2011, Borck et al., 2011, Handley & Sheridan, 2018, Liegel et al.,

106 2013)(MIMs 600118, 614222, 614225, 615663, 212720). *RAB3GAP1* and

107 *RAB3GAP2* encode subunits of the binary RAB18-GEF complex, 'RAB3GAP',

108 whereas *TBC1D20* encodes a RAB18-GAP (Gerondopoulos et al., 2014, Handley et

109 al., 2015). Thus, the same pathology is produced when functional RAB18 is absent

110 or when its normal regulation is disrupted. However, it is unclear how RAB18

111 dysfunction contributes to disease pathology at a molecular level.

112 Rab proteins fulfil their roles by way of protein-protein interactions with interacting

113 partners termed 'effectors'. The identification of these proteins can therefore provide

114 insight into these roles. However, biochemical identification of Rab effectors is

115 challenging; Rab-effector interactions are usually GTP-dependent and are often

116 highly transient. Immunoprecipitation, affinity purification and yeast-2-hybrid

117 approaches have each been used, but may be more or less effective depending on

118 the Rab isoform studied (Christoforidis et al., 1999, Fukuda et al., 2008).

119 One newer approach is 'BioID' proximity biotinylation utilizing Rab proteins fused to

120 mutant forms of the biotin ligase BirA. The Rab fusion protein biotinylates proximal

121 proteins which are then purified on streptavidin and identified through mass

122 spectrometry (Gillingham et al., 2019, Liu et al., 2018, Roux et al., 2012). Biotin

123 labelling occurs in a relatively physiological context and prospective effectors can be

124 purified under high stringency conditions. However, a drawback of the technique is

6

125   that it does not distinguish between close associations resulting from functional

126   protein-protein interactions and those resulting from overlapping localizations.

127   To discriminate functional RAB18 interactions, we compared BirA*-RAB18 labelling

128   of protein in wild-type HeLa cells to that in cells in which RAB18-GEF activity was

129   disrupted with CRISPR. Known and novel effectors were more strongly labelled in

130   the wild-type cells. In particular, 25 RAB18-interactions were RAB3GAP-dependent.

131   These proteins comprised several groups. Proteins within each group were clearly

132   interrelated through involvement in connected biological processes. Moreover, gene-

133   disease associations within the set included multiple overlapping phenotypes. We

134   present additional evidence for several examples of RAB3GAP-dependent RAB18

135   interactions: SPG20/SPART; SEC22A; TMCO4; EBP; ORP2/OSBPL2 and INPP5B.

136   Our data elaborate an existing model suggesting that RAB18 effectors act

137   collectively in lipid transfer at membrane contact sites (Xu et al., 2018). We identify

138   multiple proteins already implicated in the establishment and maintenance of

139   membrane-contacts. Importantly, we also identify novel RAB18-interactors involved

140   in lipid biosynthesis, mobilization and metabolism. We find that RAB18 appears to

141   coordinate generation of the cholesterol precursor lathosterol by the Δ8-Δ7 sterol

142   isomerase enzyme EBP, and its subsequent mobilization by the lipid transfer protein

143   (LTP) ORP2/OSBPL2. Consistently, cholesterol biosynthesis is impaired in model

144   cell lines lacking RAB18 or its regulators. Taken together, these findings suggest that

145   Micro syndrome is a cholesterol biosynthesis disorder. Further, that therapeutic

146   interventions might be feasible in this disease.

147   RESULTS

148

149   An inventory of RAB18-GEF-dependent RAB18-associated proteins in HeLa cells

150   We first used CRISPR to generate a panel of clonal, otherwise isogenic, HeLa cell

151   lines null for RAB18 and a number of its regulators (see Figure S1). We then carried

152   out proximity labelling using transient expression of the same exogenous BirA*-

153   RAB18 construct in RAB3GAP1-, RAB3GAP2- and TRAPPC9-null cell lines and in

154   wild-type cells (Figure 1A). RAB3GAP1 and RAB3GAP2 are each essential subunits

155   of a binary RAB18-GEF complex (Gerondopoulos et al., 2014). TRAPPC9 is

156   reported to be essential for the RAB18-GEF activity of a different GEF, the

157   multisubunit TRAPPII complex (Li et al., 2017).

158   Proximity-labelling, affinity purification and mass spectrometry of biotinylated

159   proteins were carried out essentially as previously described (Roux et al., 2018,

160   Roux et al., 2012). Prior to mass-spec analysis, samples from each of the

161   streptavidin pull-downs were subjected to Western blotting to ensure comparable

162   BirA*-RAB18 expression (Figure S2A). Label-free quantitative proteomics analyses

163   were used to calculate 'LFQ intensities' for each RAB18-associated protein (Cox et

164   al., 2014). These were then normalized in each experiment according to the quantity

165   of RAB18 found in each sample. Samples from three independent experiments were

166   analysed. Pull-downs from untransfected biotin-treated cells were used as controls.

167   After filtering the data to remove known mass-spec contaminants and any protein

168   identified at a high level in control samples, a total of 584, 483 and 506 RAB18-

169   associated proteins were identified in each experiment. A total of 457 proteins were

170   present in two or more of the replicate experiments (see Table S1).

171   Different Rab-GEF complexes may operate in distinct subcellular localizations and

172   coordinate associations with different effectors (Carney et al., 2006). Therefore, we

173   assessed whether non-zero intensities for each RAB18-associated protein correlated

174   between samples (Figure 1B, Figure S2B). Very strong correlations between protein

175   intensities from RAB3GAP1- and RAB3GAP2-null cells indicated that loss of either

176   protein had a functionally equivalent effect (R^2=0.99, Figure 1B). In contrast,

177   intensities from RAB3GAP1/2- and TRAPPC9-null cells were much more poorly

178   correlated (R^2=0.73, R^2=0.74, Figure S2B). We therefore considered RAB3GAP- and

8

179   TRAPPC9-dependent RAB18-interactions separately. Intensities from wild-type and

180   RAB3GAP-null samples correlated with an R^2=0.87, but a number of proteins

181   showed reduced intensities in the RAB3GAP-null samples (Figure 1C).

182   GEF activity promotes Rab GTP binding and this is usually necessary for effector

183   interactions. We therefore reasoned that levels of true effector proteins would be

184   reduced in samples from GEF-null cells as compared to those from wild-type cells.

185   We calculated GEF-null:wild-type intensity ratios for each RAB18-associated protein

186   (Table S1). Only 25 proteins showed a RAB3GAP-null:wild-type ratio <0.5 (Figure

187   1D, Table 1, Table S1). 133 proteins showed a TRAPPII-null:wild-type intensity ratio

188   <0.5 (Figure 1D, Table S1). There was only limited overlap between RAB3GAP- and

189   TRAPPC9-dependent associations (Figure 1D).

190   The most comprehensive annotation of candidate RAB18 effectors thus far was

191   made in the 2014 paper by Gillingham et al., which utilized an affinity purification-

192   mass spectrometry (AP-MS) approach and the *Drosophila* RAB18 orthologue

193   (Gillingham et al., 2014). In that study, a total of 456 proteins were identified as

194   interacting with RAB18. However, only 14 of these were well represented in terms of

195   spectral counts, exhibited low non-specific binding to GST/sepharose and showed

196   low binding to other Rab protein isoforms. We took these 14 proteins as the most

197   plausible physiological RAB18 interactors and searched for these in our datasets.

198   Orthologues of 11 of the 14 putative RAB18-interacting proteins identified by

199   Gillingham et al. were identified in our combined dataset. 10/14 were among the 25

200   RAB3GAP-dependent associations (Table 1). 2/14 were among the TRAPPII-

201   dependent associations (Table S1).

202   For initial validation of our dataset, we carried out an additional independent BioID

203   experiment with wild-type and RAB3GAP1-null cells and subjected the resulting

204   samples to Western blotting for selected RAB18-associated proteins (Figure 1E). As

205   with the mass spectrometry, these proteins showed either complete (RAB3GAP1,

206   RAB3GAP2, ZW10) or partial (SPG20, STX18) dependence on RAB3GAP for their

207   RAB18 association.

208   We further validated our approach with additional proximity biotinylation experiments

209   in HEK293 cells. We used cells stably expressing BirA*-tagged RAB18 fusions

210   incorporating wild-type RAB18, GTP-hydrolysis deficient RAB18(Gln67Leu), or

211   nucleotide-binding deficient RAB18(Ser22Asn) mutants (Figure S3A-B). A total of 98

212   proteins were identified as associating with RAB18 across all samples (Table S2).

213   Gln67Leu:wild-type intensity ratios for known RAB18-interactors ranged from 0.1-

214   1.49 indicating that RAB18 associations were altered by the Gln67Leu variant, but

215   not predictably so. In contrast, Ser22Asn:wild-type intensity ratios were <0.5 for the

216   majority of these proteins. 28 nucleotide-binding-dependent RAB18 associations

217   included 6 of the RAB3GAP-dependent associations and 7 of the TRAPPII-

218   dependent associations seen in the HeLa cells (Figure S3C). These data confirm

219   that the loss of GEFs has similar effects on RAB18-interactions to direct loss of

220   nucleotide binding. In addition, they support the differing regulation of specific

221   RAB18-interactions by different GEFs.

222

223   <u>Validation screening of RAB3GAP-dependent RAB18 associations reveals reduced</u>

224   <u>levels of SPG20 in RAB18-null and TBC1D20-null cells</u>

225   Our continued study focused on the 25 RAB3GAP-dependent RAB18 associations

226   identified in HeLa cells. Encouragingly, these appeared to share interconnected

227   functions and fell into discrete groups (Table 1). Furthermore, genes encoding 11 of

228   the 25 proteins or their homologues are associated with inherited diseases that

229   share features with Micro syndrome (Table 2).

230   Given the suggestive convergences in protein function and gene-disease-

231   associations, we examined the subcellular localizations of 12 putative effectors for

232   which antibodies were available (Figure 2A-B). To determine whether the localization

233   of these proteins was altered in cells lacking RAB18, we analysed wild type and

234   RAB18-null lines in each case. In order to directly compare cells of different

235   genotypes under otherwise identical conditions, we labelled them with CellTrace-

236   Violet and CellTrace-Far Red reagents before seeding, immunostaining and imaging

237   them together. Since RAB18 can localize to lipid droplets (LDs), we analysed both

238   untreated cells (Figure 2A) and cells loaded with oleic acid and labelled with

239   BODIPY-558/568-C12 (Figure 2B).

240   The putative effector proteins showed various staining patterns. These ranged from

241   staining that was enriched at the perinuclear region of cells, to staining that appeared

242   reticular, to staining that appeared more diffuse. Staining patterns were similar in the

10

243   HeLa cells and also in RPE1 cells generated to provide biological replicates (Figure

244   S4A). Each pattern was compatible with the known localization of RAB18, which is

245   distributed between *cis*-Golgi, ER and cytosolic compartments (Handley et al., 2015).

246   In lipid-loaded cells, localizations of proteins with reticular staining patterns

247   overlapped with LDs but they did not obviously shift to adopt a LD localization. Two

248   proteins that showed diffuse staining patterns in untreated cells - ZW10 and SPG20 -

249   appeared enriched in the vicinity of LDs (Figure 2B, bottom right panels).

250   We saw no evidence for dramatic changes in protein localizations in RAB18-null

251   cells as compared to their wild-type counterparts. Fluorescence intensities in RAB18-

252   null and wild-type cells were also generally similar, except in the case of staining for

253   SPG20, which appeared lower in RAB18-null HeLa cells than in wild-type cells

254   (Figure 2A, bottom right panels).

255   To confirm the reduction in levels of SPG20 we observed in RAB18-null HeLa cells

256   and to determine the effects of other genotypes, we used quantitative fluorescence

257   microscopy (Figure 2C). To establish SPG20 antibody specificity we first analysed

258   SPG20-null cells (Figure 2D, left panels). Measured fluorescence intensity of these

259   cells also provided a baseline level, above which fluorescence levels are proportional

260   to levels of SPG20 (Figure 2E). In RAB18-null cells, SPG20 fluorescence was

261   reduced to 67.16±3.77% (p<0.001) of that in wild-type cells (Figure 2F). Loss of the

262   RAB18-GEF subunits RAB3GAP1 or RAB3GAP2 did not significantly affect levels of

263   SPG20, whereas loss of the RAB18-GAP TBC1D20 led to a reduction comparable to

264   that in RAB18-null cells (57.48%±2.57, p<0.00005)(Figure 2F).

265   We analysed levels of SPG20 in the corresponding panel of RPE1 cell lines using

266   LFQP analysis of whole cell lysates (Figure S4B, Table S3). As in the HeLa cells,

267   levels of SPG20 were significantly reduced in RAB18- and TBC1D20-null RPE1 cells

268   compared to wild-type controls (p<0.05 following FDR correction), but not in the

269   other genotypes tested. These data suggest that reduced SPG20 levels result from

270   specific genotypes and are not the result of clonal variation. A comparison between

271   LFQP data from wild-type and TBC1D20-null RPE1 and HeLa cells (Tables S3 and

272   S4) showed limited overlap between differentially expressed proteins. This indicates

273   that reduced SPG20 levels are unlikely to have resulted from widespread

274   dysregulation of proteostasis. The RAB18-SPG20 interaction has been previously

11

275   reported (Gillingham et al., 2014), and our findings (above) provide further support

276   for a physiological relationship between these proteins.

277

278   <u>SEC22A associates with RAB18 and its knockdown causes altered LD morphology</u>

279   The most studied group of RAB18 effector proteins to date are the tethering factors

280   that comprise the NRZ/Dsl complex (ZW10, NBAS and RINT1), and the ER SNARE

281   proteins that comprise the Syntaxin18 complex (STX18, BNIP1, USE1 and SEC22B)

282   (Gillingham et al., 2014, Li et al., 2019, Xu et al., 2018, Zhao & Imperiale, 2017).

283   Although SNARE complexes typically mediate membrane fusion, it has been

284   proposed that RAB18 interacts with these proteins to mediate the close apposition of

285   membranes to facilitate lipid transfer (Xu et al., 2018). It has also been suggested

286   that SEC22B is dispensable for this function (Xu et al., 2018).

287   Our screen for RAB3GAP-dependent RAB18-interactors identified all of the NRZ

288   complex components, as well as the SNARE proteins STX18 and BNIP1 (Table 1).

289   Interestingly, we did not identify SEC22B but did identify SEC22A among these

290   proteins. SEC22A is one of the two SEC22B homologues in humans that lack the

291   central coiled-coil SNARE domain through which SEC22B mediates membrane

292   fusion (Rossi et al., 2004). Since it had not been previously described as a RAB18-

293   interacting protein, we investigated this further.

294   In the absence of commercially available antibodies for SEC22A, we examined its

295   localization through expression of a mEmerald-SEC22A fusion protein (Figure 3A).

296   mEmerald-SEC22A produced a characteristic reticular staining pattern and

297   colocalized with an exogenous ER marker suggesting that SEC22A localizes to the

298   ER. We next sought to compare the localization of SEC22A and RAB18 and to

299   determine whether they interact. However, coexpression of mEmerald-SEC22A and

300   mCherry-RAB18 disrupted normal ER morphology produced vesicular structures and

301   inclusions positive for both proteins (Figure S5). Although this was not inconsistent

302   with a protein-protein interaction, it precluded the use of coexpressed exogenous

303   proteins in continued testing.

304   As an alternative means of assessing SEC22A-interactions, we used proximity

305   biotinylation with a BirA*-SEC22A fusion protein in the HeLa cell panel. To minimize

306   potential toxicity while increasing biotin-ligase activity, we used BioID2 (Kim et al.,

307   2016) with a p.Gly40Ser active site modification (Branon et al., 2018) and reduced

308   biotin incubation time. Despite a low level of BioID2(Gly40S)-SEC22A expression,

309   the construct appeared to label RAB18 in a RAB3GAP-dependent manner (Figure

310   3B). 55 SEC22A-associated proteins were present in samples from wild-type cells in

311   >2 replicate experiments and represented by >3 spectral counts (Table S5). Further,

312   a subset of 9 SEC22A-associations were attenuated (intensity ratios <0.5) in

313   samples from both RAB18-null and RAB3GAP-null cells. These data are consistent

314   with a physiological SEC22A-RAB18 interaction.

315   A phenotype of altered LD morphology in lipid-loaded cells has been widely reported

316   in cells deficient in RAB18 (Bekbulat et al., 2019, Carpanini et al., 2014,

317   Gerondopoulos et al., 2014, Li et al., 2017, Liegel et al., 2013, Xu et al., 2018).

318   Similar observations have been made in cells deficient in some components of the

319   NRZ or Syntaxin18 complexes, but not in cells deficient in SEC22B (Xu et al., 2018).

320   To test whether SEC22A expression influences LD morphology, we examined the

321   effects of its silencing in oleic acid-loaded induced human hepatocyte (IHH) cells

322   (Figure 3C). ZW10 and NBAS silencing provided positive controls in our

323   experiments. ZW10 silencing led to a significant reduction in LD number (p<0.001)

324   compared to controls, whereas NBAS silencing led to both a significant reduction in

325   LD number and a significant increase in LD size (p<0.001 in each case). The effects

326   of SEC22A silencing mirrored those of NBAS silencing, producing a significant

327   reduction in LD number (p<0.001) and a significant increase in LD size (p<0.001).

328   Together, these data implicate SEC22A as involved in the same RAB18-mediated

329   process(es) as the NRZ and SNARE proteins.

330

331   RAB18 recruits the orphan lipase TMCO4 to the ER membrane in a RAB3GAP-

332   dependent manner

333   The most novel group of putative RAB18 effectors identified in our study were the

334   lipid modifying/mobilizing proteins, none of which had been reported to associate

335   with RAB18 previously. Among these, TMCO4 was identified in all three replicate

336   experiments and its association with RAB18 was highly RAB3GAP-dependent

337   (intensity ratio 0.06). Although annotated as containing transmembrane and coiled-

338   coil domains, it is orthologous to the Yeast protein Mil1/ Yfl034w, and likely to be a

13

339 partly soluble lipase (Whitfield et al., 2016). Consistently, TMCO4-EGFP expressed

340 in HeLa cells showed a diffuse localization. In contrast, EGFP-RAB18 partly localizes

341 to the ER, as shown by its colocalization with an ER marker (Figure 4A).

342 To assess the potential RAB18-TMCO4 interaction, we coexpressed mCherry-

343 RAB18 and TMCO4-EGFP (Figure 4B). As in our previous experiments, Celltrace

344 reagents were used to distinguish cells of wild-type and mutant genotypes. In wild-

345 type HeLa cells, coexpression of mCherry-RAB18 led to a dramatic redistribution of

346 TMCO4-EGFP to the ER membrane suggesting that RAB18 mediates recruitment of

347 TMCO4 to this compartment. Redistribution was completely absent in RAB3GAP1-

348 and RAB3GAP2-null cells but unaffected in TRAPPC9-null cells, consistent with the

349 BioID data.

350 As a means of verifying the RAB18-TMCO4 interaction, we carried out

351 immunoprecipitation experiments using exogenous HA-RAB18 and TMCO4-EGFP

352 (Figure 4C). As expected, TMCO4-EGFP copurified with HA-RAB18 when

353 expressed in wild-type or TRAPPC9-null cells, but not when expressed in

354 RAB3GAP1-null cells. These data indicate that RAB18 and TMCO4 interact directly

355 or indirectly as part of a protein complex in a RAB3GAP-dependent manner. Further,

356 both the microscopy and the immunoprecipitation data support the suggestion that

357 different GEFs can promote different RAB18-interactions.

358

359 <u>RAB18 is involved in cholesterol mobilization and biosynthesis</u>

360 Other putative RAB18 effectors with lipid-related functions included ORP2/OSBPL2,

361 INPP5B and EBP. ORP2 and INPP5B are robustly linked to a role in cholesterol

362 mobilization. ORP2 is thought to function as a lipid transfer protein that exchanges

363 cholesterol and PI(4,5)P$_2$ (Wang et al., 2019). INPP5B is implicated in the hydrolysis

364 of ORP2-bound PI(4,5)P$_2$, presumably driving the exchange process (Wang et al.,

365 2019). EBP is involved in *de novo* cholesterol biosynthesis (Silve et al., 1996). In the

366 Bloch pathway, it catalyses the conversion of 5α-cholesta-8, 24-dien-3β-ol

367 (zymosterol) to 5α-cholesta-7, 24-dien-3β-ol (24-dehydrolathosterol). In the

368 Kandutsch-Russel pathway, it catalyses the conversion of 5α-cholest-8(9)-en-3β-ol

369 to 5α-cholest-7-en-3β-ol (lathosterol)(Platt et al., 2014). On the basis of these

14

370   findings, we investigated the potential role of RAB18 in cholesterol uptake, efflux and

371   biosynthesis.

372   We first performed loading and efflux experiments to measure the flux of

373   cholesterol/cholesteryl ester (CE) while modifying the activity of RAB18. Chinese

374   hamster ovary (CHO) cells were generated to stably express RAB18(WT),

375   RAB18(Gln67Leu), or RAB18(Ser22Asn) (Figure S6A). In cells labelled with [^{14}C]-

376   oleate, but cholesterol depleted with lipoprotein-depleted serum (LPDS), levels of CE

377   were comparable in RAB18(Ser22Asn) and RAB18(WT) cells, whereas

378   RAB18(Gln67Leu) cells stored significantly more (Figure 5A, left panel). In cells

379   labelled with [^{14}C]-oleate and cholesterol-loaded FBS, levels of CE in

380   RAB18(Ser22Asn) remained unchanged, whereas its storage was elevated in

381   RAB18(WT) cells and RAB18(Gln67Leu) cells (Figure 5A, right panel). Interestingly,

382   in both [^{14}C]-oleate/LPDS and [^{14}C]-oleate/FBS cells, the addition of high density

383   lipoprotein (HDL, a vehicle mediating removal of cellular cholesterol) led to rapid

384   depletion of CE in RAB18(Gln67Leu) cells, but not in RAB18(Ser22Asn) or

385   RAB18(WT) cells (Figure 5A). Consistently, RAB18(Gln67Leu) cells also effluxed

386   significantly more [^{3}H]-cholesterol upon their incubation with apolipoprotein (apo) A-I

387   than the other cell types (Figure 5B). These observations were not explained by

388   altered expression of ABCA1, the transporter responsible for the rate-limiting step of

389   cholesterol efflux (Figure S6B). These data suggest that 'activated' GTP-bound

390   RAB18 strongly promotes the storage, turnover and mobilization of CE stored in

391   LDs. A plausible explanation for this is that active RAB18 promotes cholesterol

392   mobilization via ORP2 and INPP5B.

393   Given that ORP2 and INPP5B function in sterol mobilization whereas EBP functions

394   in sterol biosynthesis, we reasoned that RAB18 might coordinate their activities; that

395   ORP2 might act as an exchanger for the substrates or products of EBP-catalysis as

396   well as for cholesterol. In this case, defective mobilization of cholesterol precursors

397   might lead to their accumulation in RAB18-null cells. To test this hypothesis, we

398   incubated wild-type and RAB18-null cells for 48 hours in media supplemented with

399   LPDS, then subjected samples to analysis by GC-MS (Figure 5C-D). In RAB18-null

400   cells, we found that levels of the EBP-substrate cholest-8(9)-en-3β-ol were not

401   significantly different from those in wild-type cells. In contrast, levels of EBP-product

402   lathosterol were significantly increased (p<0.01). This suggests that RAB18

15

403   facilitates ORP2-mediated mobilization of lathosterol away from the site of its

404   generation by EBP. Consistently, levels of desmosterol - downstream of 24-

405   dehydrolathosterol in the Bloch pathway - were significantly reduced in RAB18-null

406   cells (p<0.01). These data suggest that delivery of substrates to post-EBP

407   biosynthetic enzymes is impaired.

408   To further test our hypothesis, we used molecular dynamics (MD) simulations to

409   model lathosterol binding to ORP2. We compared simulations of the ORP2 OSBP-

410   related domain (ORD) incorporating cholesterol and lathosterol over 1μs (Figure 5E-

411   G, Figure S7, Videos S1-2). Over this time, both simulations remained comparatively

412   stable in terms of positional root-mean-square deviation (RMSD) (Figure S7A), with

413   both termini highly dynamic. The pattern of positional root-mean-square fluctuations

414   (RMSFs) for atoms in each sterol showed higher conformational heterogeneity for

415   bound lathosterol than bound cholesterol, suggesting a less constrained interaction

416   (Figure S7B). RMSFs for the ORP2-ORD amino acid residues show similar patterns

417   for the two systems, although Tyr52 (Tyr110 in NP_653081), proximal to the sterol 3-

418   hydroxyl, fluctuated less in the presence of lathosterol (Figure 5E). This residue

419   appeared differently oriented with respect to the sterol in each simulation (Figure 5F,

420   Videos S1-2). Indeed, for a large proportion of the span of the simulation with

421   lathosterol, the Tyr52 hydroxyl and the sterol 3-hydroxyl were located close together

422   and this distance remained relatively stable (Figure 5G).

423   In crystal structures of sterols with the OSBP-related protein Osh4, water-mediated

424   interactions were prominent (Im et al., 2005). Therefore, we explored whether

425   positioning of water molecules might differ between the two simulations.

426   Interestingly, we found that water molecules were more frequently found in close

427   proximity to lathosterol than the cholesterol (Figure S7C). Together, the MD

428   simulations suggest that the ligand-binding tunnel of the ORP2-ORD adopts distinct

429   conformations when bound to lathosterol or cholesterol despite their minor structural

430   differences. The interactions appear relatively stable in each case, but speculatively,

431   the interaction with lathosterol may be more entropically favourable.

432   We next reasoned that impaired delivery of substrates to post-EBP enzymes might

433   reduce cholesterol biosynthesis in cells in which RAB18 is absent or dysregulated.

434   To explore this possibility, we cultured the panel of HeLa cell lines for 24 hours in

435   media supplemented with LPDS, treated them for 24 hours with [3H]-mevalonate or

16

436   [^{3}H]-acetate, then quantified labelled cholesterol (Figure 5H). Under both conditions,

437   labelling in two clonal wild-type controls was comparable, but was reduced in

438   RAB18-, RAB3GAP1-, RAB3GAP2-, TBC1D20- and TRAPPC9-null cells. Labelling

439   was lowest in the RAB18-null cells (39.5±2.5% and 6.8±0.5% of controls for [^{3}H]-

440   mevalonate and [^{3}H]-acetate respectively). Levels in the cells of other genotypes

441   were between 46±2.5%-73±5% for [^{3}H]-mevalonate and 23±2%-43±3%±.0.5% for

442   [^{3}H]-acetate. These data strongly suggest that RAB18 and its regulators are required

443   for normal cholesterol biosynthesis.

DISCUSSION

444

445 In this study, we have complemented previous work showing that proximity

446 biotinylation is a powerful means of identifying candidate Rab effectors (Gillingham

447 et al., 2019). Further – at least in the case of RAB18 - we have found that comparing

448 biotin-labelling produced by a BirA*-Rab in wild-type and GEF-deficient cells can be

449 particularly informative. We found that marked reductions in RAB18-association in

450 RAB3GAP-null cells were restricted to only 25 proteins and that these comprised

451 known and/or plausible effectors. We were able to exclude ~95% of RAB18-

452 associations from consideration as more likely to represent 'noise' from bystander

453 proteins.

454 Prior evidence supported 12 of the 25 interactions we detected. Independent

455 experiments with a mutant RAB18 fusion protein confirmed nucleotide-binding-

456 dependence of several interactors, and immunofuorescence confirmed compatible

457 localizations of several more. The known functions of the proteins were consistent

458 with previous work implicating RAB18 in coordination of lipid exchange between

459 apposed membranes (Xu et al., 2018). Further, gene-disease associations showed

460 substantial overlap with RAB18-deficiency/Warburg Micro syndrome. We have

461 presented additional validation for six interactions, five of which are novel.

462 Our protein-interaction data implicate RAB18 in regulation of a stepwise process in

463 which membrane/cytoskeletal remodelling precedes the engagement of tethering

464 proteins and then SNAREs to establish membrane contact sites. At these sites, it

465 then appears to couple the generation of lathosterol by EBP and its subsequent

466 mobilization and delivery to downstream biosynthetic enzymes. The effectors most

467 directly responsible for sterol mobilization are likely to be ORP2 and INPP5B. We

468 propose that RAB18, ORP2 and INPP5B function in an analogous manner to the

469 well studied ARF1-OSBP-SACM1L axis (Antonny et al., 2018). The GTPase

470 (RAB18/ARF1) facilitates ORP (ORP2/OSBP)-mediated exchange of sterol

471 (lathosterol/cholesterol) and phosphatidylinositde (PI(4,5)P_2/PI(4)P) between

472 apposed membranes. The phosphatase (INPP5B/SACM1L) acts to maintain the

473 necessary phosphoinositide concentration gradient (Figure 6).

474 The role of Rab proteins in mediating vesicular membrane trafficking is well known.

475 Emerging evidence also suggests that regulation of nonvesicular lipid exchange at

18

476   membrane contact sites may likewise be a broadly conserved function. Several Rab

477   isoforms are shown to interact with ORPs (Gillingham et al., 2019, Levin-Konigsberg

478   et al., 2019, Rocha et al., 2009, Sobajima et al., 2018). Many are also found to

479   interact with phospholipid phosphatases, including phosphatases from distinct

480   protein families (Fukuda et al., 2008, Gillingham et al., 2019, Williams et al., 2007).

481   Thus, the large number of possible GTPase-OSBP-phosphatase combinations

482   provides a potential means to orchestrate mobilization of a multitude of lipid species.

483   In this context, our finding that RAB18 also interacts with a biosynthetic enzyme and

484   mediates mobilization of a specific sterol intermediate is suggestive. The connection

485   between the enzyme and the mobilization machinery provides a mechanism

486   conferring increased selectivity for the lipid cargo (Nishimura & Stefan, 2020).

487   Resolving the functional and compositional diversity of membrane contact sites is a

488   challenge for future research. Similarly, the scope and precise mechanics of RAB18-

489   regulated lipid exchange are not yet understood. Although our experiments have

490   helped to validate our proximity-labelling approach, the roles of most of the RAB18-

491   effectors identified require additional analyses. Among the lipid-related proteins,

492   TMCO4 may potentially be directly or indirectly associated with sterol metabolism.

493   Although its substrate(s) are unknown, its expression is found to be upregulated in

494   hypercholesterolemia (Ong et al., 2013) and it is present on lipid rafts (Jin et al.,

495   2012). The remaining lipid-related proteins, C2CD2L/TMEM24 and C2CD2, might

496   potentially function in concert with ORP2 and/or INPP5B, since C2CD2L is found to

497   mediate PI transport and to facilitate generation of PI(4,5)P$_2$ (Lees et al., 2017).

498   The possible substitution of SEC22B for SEC22A in a RAB18-regulated Syntaxin18

499   SNARE complex (Figure S8A), and a possible role for this complex in promoting

500   membrane contacts rather than membrane fusion, is consistent with previous data

501   (Xu et al., 2018). Further, it would be in keeping with roles for the NRZ/Dsl1 complex

502   and SCFD2/Sly1 in dynamically orchestrating SNARE complex assembly (Ren et al.,

503   2009, Spang, 2012, Yamaguchi et al., 2002). More ambiguously, the RAB18-

504   interacting microtubule binding proteins have not previously been reported to work

505   together but do function in compatible locations (Figure S8B). SPG20 and

506   CAMSAP1 each associate with mitotic spindle poles, REEP4 participates in spindle-

507   dependent ER clearance from metaphase chromatin and BICD2 is a component of

508   the minus-end-directed dynein-dynactin motor complex (Hendershott & Vale, 2014,

509   Hueschen et al., 2017, Kumar et al., 2019, Lind et al., 2011, Nicholson et al., 2015,

510   Schlaitz et al., 2013, Urnavicius et al., 2015). Our TRAPPII-dependent RAB18

511   interaction data indicate that different GEF complexes affect largely distinct subsets

512   of interactions. However, more work will be required to determine whether these

513   regulators mediate independent or interdependent functions.

514   Our objective in studying RAB18 was to better understand the molecular pathology

515   of Warburg Micro syndrome. Though our protein-interaction data are relatively

516   preliminary, our functional findings represent good progress towards this goal. Our

517   key finding is that disrupted *de novo* cholesterol biosynthesis may contribute to

518   disease pathogenesis. Strongly supporting this suggestion, genes encoding multiple

519   cholesterol biosynthesis enzymes are linked to similar disorders (Platt et al., 2014).

520   For example, pathogenic variants in the lathosterol oxidase gene, *SC5D*, cause

521   lathosterolosis, which is associated with microcephaly, intellectual disability,

522   micrognathia, high arched palate and cataract (Anderson et al., 2019, Brunetti-Pierri

523   et al., 2002, Ho et al., 2014, Krakowiak et al., 2003, Rossi et al., 2007). Pathogenic

524   variants in the 7-dehydrocholesterol reductase gene, *DHCR7*, cause Smith-Lemli-

525   Opitz syndrome (SLOS), which has a similar spectrum of features and is among the

526   top differential diagnoses for Micro syndrome (Handley & Sheridan, 2018, Nowaczyk

527   & Wassif, 1998). Indeed, the similarities with SLOS were noted in the report first

528   identifying RAB18 as a disease-associated gene nearly a decade ago (Bem et al.,

529   2011).

530   Therapeutics have been trialled in lathosterolosis and SLOS. Cholesterol

531   supplementation has been widely used and more recently is being combined with

532   antioxidants with the aim of reducing toxicity from aberrant cholesterol metabolites

533   (Fliesler et al., 2018, Korade et al., 2014, Svoboda et al., 2012). Additionally,

534   paradoxical treatment with statins may increase the expression of sterol synthesizing

535   enzymes (Correa-Cerro et al., 2006, Ho et al., 2014, Jira et al., 1997, Wassif et al.,

536   2017). Careful clinical research will be required to determine the safety and efficacy

537   of such interventions in Warburg Micro syndrome.

538   MATERIALS AND METHODS

539

540   Plasmids

541   The EGFP-RAB18 construct has been described previously (Gerondopoulos et al.,

542   2014). The RAB18 sequence was excised from this construct using BamHI and

543   HindIII restriction enzymes (New England Biolabs, Hitchin, UK), and used to

544   generate constructs encoding mEmerald-RAB18 and mCherry-RAB18 by ligation

545   into mEmerald-C1 and mCherry-C1 vectors (Addgene, Watertown, MA) using HC T4

546   Ligase and rapid ligation buffer (Promega, Southampton, UK). Constructs encoding

547   BirA*-RAB18, BioID2(Gly40Ser)-SEC22A and mEmerald-SEC22A were generated

548   following PCR amplification from template and subcloning into an intermediate pCR-

549   Blunt II-TOPO vector using a Zero Blunt TOPO PCR Cloning Kit (ThermoFisher

550   Scientific, Waltham, MA) according to manufacturer's instructions. Fragments were

551   excised from intermediate vectors and then subcloned into target vectors using

552   restriction-ligation, as above. A construct encoding mCherry-ER was obtained from

553   Addgene, and a construct encoding TMCO4-EGFP was synthesised and cloned by

554   GeneWiz (Leipzig, Germany). Generation of recombinant pX461 and pX462

555   plasmids for CRISPR gene-editing, and recombinant pCMV vectors for preparation

556   of stable CHO cell lines are described below. Generation of recombinant pcDNA5

557   FRT/TO FLAG-BirA(Arg118Gly) vectors for preparation of stable T-Rex-293 cell lines

558   is described in supplementary methods. Details of PCR templates, primers and

559   target vectors are listed in Table S6.

560

561   Antibodies and reagents

562   A custom polyclonal antibody to RAB18 generated by Eurogentec (Southampton,

563   UK) has been described previously (Handley et al., 2015). An antibody to

564   RAB3GAP1 was obtained from Bethyl Labs (Montgomery, TX), an antibody to GFP

565   was obtained from Takara Bio (Saint-Germain-en-Laye, France), an antibody to β-

566   Tubulin was obtained from Abcam (Cambridge, UK) and an antibody to β-Actin was

567   obtained from ThermoFisher. Antibodies to hemagglutinin (HA), RAB3GAP2 and

568   TBC1D20 were obtained from Merck (Gillingham, UK). Antibodies to ZW10, STX18,

569   SPG20, RINT1, REEP4, BNIP1, C2CD2, TRIM13, WFS1, INPP5B, OSBPL2 and

21

570 NBAS were obtained from Proteintech (Manchester, UK). Antibody catalogue

571 numbers and the dilutions used in this study are listed in Table S6.

572

573 <u>Cell culture</u>

574 HeLa, T-REx-293 and IHH cells were maintained in DMEM media, RPE1 cells in

575 DMEM/F12 media and CHO cells in alpha-MEM media (ThermoFisher). In each

576 case, media was supplemented with 10% foetal calf serum (FCS) and 1% penicillin-

577 streptomycin (PS). Cells were maintained at 37°C and 5% CO_2.

578

579 <u>Generation of clonal 'knockout' HeLa and RPE1 cell lines</u>

580 CRISPR/Cas9 gene-editing was carried out essentially as described in Ran et al.,

581 2013 (Ran et al., 2013). Guide RNA (gRNA) sequences are shown in Table S6. A list

582 of the clonal cell lines generated for this study, together with the loss-of-function

583 variants they carry is shown in Figure S1A. Western blot validation is shown in

584 Figure S1B-E. Briefly, for each targeted exon, pairs of gRNA sequences were

585 selected using the online CRISPR design tool (http://crispr.mit.edu/). Oligonucleotide

586 pairs incorporating these sequences (Sigma) were annealed (at 50mM ea.) in 10mM

587 Tris pH8, 50mM NaCl and 1mM EDTA by incubation at 95ºC for 10 minutes followed

588 by cooling to room temperature. Annealed oligonucleotides were diluted and ligated

589 into BbsI-digested pX461 and pX462 plasmids (Addgene) using HC T4 Ligase and

590 rapid ligation buffer (Promega). Sequences of all recombinant plasmids were verified

591 by direct sequencing. Pairs of plasmids were contransfected into cells using

592 Lipofectamine 2000 reagent according to manufacturer's instructions. Cells were

593 selected for puromycin resistance (conferred by pX462) using 24 hours puromycin-

594 treatment. Following 12 hours recovery, they were selected for GFP fluorescence

595 (conferred by pX461) and cloned using FACSAria2 SORP, Influx or FACSMelody

596 instruments (BD, Wokingham, UK). After sufficient growth, clones were analysed by

597 PCR of the targeted exons (Primers are listed in Table S6). In order to sequence

598 individual gene-edited alleles, PCR products from each clone were first cloned into

599 ZeroBlunt TOPO vector (ThermoFisher) and then subjected to colony PCR. These

600 PCR products were then analysed by direct sequencing. Sequencing data was

601 assessed using BioEdit software (http://www.mbio.ncsu.edu/BioEdit/bioedit.html).

22

602   BirA*/BioID proximity labelling (HeLa cells)

603   Proximity-labelling in HeLa cells was carried out largely as described by Roux et al.

604   (Roux et al., 2012), but with minor modifications. HeLa cells were grown to 80%

605   confluence in T75 flasks and then each flask was transfected with 1-1.5µg of the

606   BirA*-RAB18 construct or 1µg of the BioID2(Gly40Ser)-SEC22A construct using

607   Lipofectamine 2000 reagent in Optimem serum-free medium (ThermoFisher) for 4

608   hours, according to manufacturer's instructions. 24 hours post-transfection, media

609   was replaced with fresh media containing 50µM Biotin (Merck) and the cells were

610   incubated for a further 24 or 6 hours (for BirA*-RAB18 and BioID2(Gly40Ser)-

611   SEC22A experiments respectively). Cells were then trypsinised and washed twice in

612   PBS before pellets were transferred to 2ml microcentrifuge tubes and snap-frozen.

613   For each pellet, lysis was carried out in 420µl of a buffer containing 0.2% SDS, 6%

614   Triton-X-100, 500mM NaCl, 1mM DTT, EDTA-free protease-inhibitor solution

615   (Expedeon, Cambridge, UK), 50mM Tris pH7.4. Lysates were sonicated for 10

616   minutes using a Bioruptor device together with protein extraction beads (Diagenode,

617   Denville, NJ). Each lysate was diluted with 1080µl 50mM Tris pH7.4, and they were

618   then clarified by centrifugation at 20 000xg for 30 minutes at 4ºC. Affinity purification

619   of biotinylated proteins was carried out by incubation of clarified lysates with

620   streptavidin-coated magnetic Dynabeads (ThermoFisher) for 24 hours at 4ºC. Note

621   that a mixture of Dynabeads - MyOne C1, MyOne T1, M270 and M280 – was used

622   to overcome a problem with bead-clumping observed when MyOne C1 beads were

623   used alone. Successive washes were carried out at room temperature with 2% SDS,

624   a buffer containing 1% Triton-X-100, 1mM EDTA, 500mM NaCl, 50mM HEPES

625   pH7.5, a buffer containing 0.5% NP40, 1mM EDTA, 250mM LiCl, 10mM Tris pH7.4,

626   50mM Tris pH7.4, and 50mM ammonium bicarbonate.

627

628   Mass spectrometry

629   Washed beads from BioID experiments with HeLa cells were subjected to limited

630   proteolysis by trypsin (0.3 µg) at 27°C for 6.5hours in 2mM urea, 1mM DTT, 75mM

631   Tris, pH=8.5, then supernatants were incubated overnight at 37°C. Samples were

632   alkylated with 50mM iodoacetamide (IAA) in the dark for 20minutes, then acidified by

633   addition of 8µl 10% trifluoroacetic acid (TFA).

634   Peptides were loaded on to activated (methanol), equilibrated (0.1% TFA) C18 stage

635   tips before being washed with 0.1% TFA and eluted with 0.1% TFA/80 acetonitrile.

636   The organic was dried off, 0.1% TFA added to 15 µl and 5 µl injected onto LC-MS.

637   Peptides were separated on an Ultimate nano HPLC instrument (ThermoFisher), and

638   analysed on either an Orbitrap Lumos or a Q Exactive Plus instrument

639   (ThermoFisher). After data-dependent acquisition of HCD fragmentation spectra,

640   data were analysed using MaxQuant and the uniprot human reference

641   proteome. Versions, releases, parameters and gradients used for separation are

642   provided in Table S6.

643

644   Cell labelling

645   In order to distinguish cells of different genotypes within the same well/on the same

646   coverslip, CellTrace Violet and CellTrace Far Red reagents (ThermoFisher) were

647   used to label cells before they were seeded. Cells of different genotypes were first

648   trypsinised and washed with PBS separately. They were then stained in suspension

649   by incubation with either 1µM CellTrace Violet or 200nM CellTrace Far Red for 20

650   minutes at 37°C. Remaining dye was removed by addition of a ten-fold excess of full

651   media, incubation for a further 5 minutes, and then by centrifugation and

652   resuspension of the resulting pellets in fresh media. Differently-labelled cells were

653   combined prior to seeding.

654

655   Immunofluorescence microscopy

656   Cells were seeded in 96-well glass-bottom plates (PerkinElmer, Waltham, MA)

657   coated with Matrigel (Corning, Amsterdam, Netherlands) according to manufacturer's

658   instructions, and allowed to adhere for 48 hours prior to fixation. In lipid-loading

659   experiments, cells were treated with 200µM oleic acid complexed to albumin (Merck)

660   and 1µg/ml BODIPY-558/568-C12 (ThermoFisher) for 15 hours prior to fixation. Cells

661   were fixed using a solution of 3% deionised Glyoxal, 20% EtOH, 0.75% acetic acid,

662   pH=5 (Richter et al., 2018), for 20 minutes at room temperature. They were then

663   washed with PBS containing 0.9mM $CaCl_2$ and 0.5mM $MgCl_2$ and blocked with a

664   sterile-filtered buffer containing 1% Milk, 2% donkey serum (Merck), 0.05% Triton-X-

665   100 (Merck), 0.9mM $CaCl_2$ and 0.5mM $MgCl_2$ in PBS pH=7.4 for at least 1 hour prior

666 to incubation with primary antibody. Primary antibodies were added in blocking buffer

667 without Triton-X-100, and plates were incubated overnight at 4ºC. Antibody dilutions

668 are listed in Table S6. Following washing in PBS, cells were incubated with 1:2000

669 Alexa 488-conjugated secondary antibody (ThermoFisher) in blocking buffer at room

670 temperature for 1-2 hours. Following further washing in PBS, cells were imaged

671 using an Operetta High Content Imaging System (PerkinElmer) equipped with

672 Harmony software. In comparative fluorescence quantitation experiments, at least 18

673 frames – each containing >5 wild-type and >5 mutant cells – were analysed per

674 genotype. ImageJ software was used to produce regions of interest (ROIs)

675 corresponding to each cell using thresholding tools and images from the 405nm and

676 645nm channels. Median 490nm fluorescence intensity was measured for each cell

677 and mutant fluorescence intensity (as %wild-type) was calculated for each frame and

678 combined for each genotype.

679

680 Confocal microscopy – Live cell imaging

681 HeLa or RPE1 cells were seeded on glass-bottom dishes (World Precision

682 Instruments, Hitchin, UK) coated with Matrigel (Corning) and allowed to adhere for

683 24 hours prior to transfection. Transfections and cotransfections were carried out

684 with 0.5µg of each of the indicated constructs using Lipofectamine 2000 reagent in

685 Optimem serum-free medium for 4 hours, according to manufacturer's instructions.

686 Media were replaced and cells were allowed to recover for at least 18 hours prior to

687 imaging. Imaging was carried out on a Nikon A1R confocal microscope equipped

688 with the Nikon Perfect Focus System using a 60× oil immersion objective with a 1.4

689 numerical aperture. The pinhole was set to airy1. CellTrace Violet was excited using

690 a 403.5nm laser, and emitted light was collected at 425–475nm. EGFP and

691 mEmerald were excited using a 488 nm laser, and emitted light was collected at

692 500–550 nm. mCherry was excited using a 561.3 nm laser, and emitted light was

693 collected at 570–620 nm. CellTrace Far Red was excited using a 638nm laser, and

694 emitted light was collected at 663-738nm.

695

696 Immunoprecipitation

25

697   HeLa cells were seeded onto 10cm dishes and allowed to adhere for 24 hours prior

698   to transfection. Transfections and cotransfections were carried out with 0.5µg of

699   each of the indicated constructs using Lipofectamine 2000 reagent in Optimem

700   serum-free medium for 4 hours, according to manufacturer's instructions. 24 hours

701   post-transfection cells were trypsinised, washed with PBS, then lysed in a buffer

702   containing 150mM NaCl, 0.5% Triton-X-100 and EDTA-free protease-inhibitor

703   solution (Expedeon), 10mM Tris, pH=7.4. Lysates were clarified by centrifugation,

704   input samples taken, and the remaining supernatants then added to 4µg rabbit anti-

705   HA antibody (Merck). After 30 minutes incubation at 4ºC on a rotator, 100µl washed

706   protein G-coupled Dynabeads (ThermoFisher) were added and samples were

707   incubated for a further 1 hour. The Dynabeads were washed x3 with buffer

708   containing 150mM NaCl, 0.1% Triton-X-100, 10mM Tris, pH=7.4, then combined with

709   a reducing loading buffer and subjected to SDS–PAGE.

710

711   Generation of stable CHO cell lines

712   A PCR product encoding mouse RAB18 was subcloned into an intermediate TOPO

713   vector using a TOPO PCR Cloning Kit (ThermoFisher) according to manufacturer's

714   instructions. The RAB18 fragment was then excised and subcloned into the pCMV

715   vector. PCR-based site-directed mutagenesis using a GeneArt kit (ThermoFisher)

716   was then used to generate pCMV-RAB18(Gln67Leu) and pCMV-RAB18(Ser22Asn)

717   constructs. CHO cells were transfected using Lipofectamine 2000 reagent

718   (ThermoFisher) and cells stably-expressing each construct were selected-for with

719   blasticidin. Under continued selection, clonal cell-lines were grown from single cells

720   and then RAB18 protein expression was assessed. Cell lines comparably expressing

721   RAB18 constructs at levels 2.5-5x higher than those wild-type cells were used in

722   subsequent experiments.

723

724   Lipid loading experiments

725   For LD number and diameter measurements, IHH cells were seeded onto glass

726   coverslips. siRNA transfections were carried out using FuGene reagent (Promega)

727   according to manufacturer's instructions. siRNAs targeting ZW10 and NBAS were

728   obtained from IDT, Coralville, IA; siRNA targeting SEC22A was obtained from

729   Horizon Discovery, Cambridge, UK. 48 hours following transfection, cells were

730   treated with 200nM BSA conjugated oleate for 24 hours. Coverslips were washed,

731   fixed with 3% paraformaldehyde and stained with 1µg/mL BODIPY and 300nM DAPI.

732   Fluorescence images were captured on a Zeiss LSM 780 confocal microscope

733   equipped with a 100x objective. Images were analysed using ImageJ software. Data

734   are derived from measurements from >100 cells/condition and are representative of

735   three independent experiments.

736   For cholesterol storage and efflux experiments with $[^{14}C]$-oleate, CHO cell lines

737   (described above) were seeded onto 12-well plates and then grown to 60-75%

738   confluence in Alpha media supplemented with 10% LPDS. Cells were grown in the

739   presence of 10% LPDS for at least 24 hours prior to the addition of oleate. 1 µCi/ml

740    $[^{14}C]$-oleate (Perkin Elmer) was added in the presence of 10% LPDS or 10% FBS for

741   24 hours. Cells were then washed and incubated with 50µg/ml HDL for 0, 4 or 8

742   hours. Cellular lipids were extracted with hexane. Lipids were then dried-down and

743   separated by thin layer chromatography (TLC) in a hexane:diethyl ether:acetic acid

744   (80:20:2) solvent system. TLC plates were obtained from Analtech, Newark, NJ.

745   Bands corresponding to cholesteryl ester (CE) were scraped from the TLC plate, and

746   radioactivity was determined by scintillation counting in a Beckman Coulter LS6500

747   Scintillation Counter using BetaMax ES Liquid Scintillation Cocktail (ThermoFisher).

748   Three independent experiments were carried out, each with four replicates of each

749   condition. Data from a representative experiment are shown.

750   For cholesterol efflux experiments with $[^3H]$-cholesterol, CHO cells were seeded onto

751   12-well plates and then grown to 60% confluence in Alpha media supplemented with

752   10% FBS. 5 µCi/ml $[^3H]$-cholesterol (PerkinElmer) was added in the presence of 10%

753   FBS. After 3x PBS washes, cells were incubated with serum-free media containing

754   25µg/ml of human apolipoprotein A-I (ApoA-I) for 5 hours. ApoA-I was a kind gift of

755   Dr. Paul Weers (California State University, Long Beach). Radioactivity in aliquots of

756   media were determined by scintillation counting in a Beckman Coulter LS6500

757   Scintillation Counter using LSC Cocktail (PerkinElmer). Cell lysates were produced

758   by addition of 0.1N NaOH for 1 hour, and their radioactivity was determined as

759   above. Cholesterol efflux was calculated as an average (+/- SD) of the % cholesterol

760   efflux (as a ratio of the media cpm/(media + cellular cpm) x 100%).

761

762 <u>Sterol analysis</u>

763 HeLa cells were grown to 80% confluence in T75 flasks, washed twice in PBS and

764 then grown for a further 48 hours in DMEM supplemented with 10% LPDS. They

765 were then trypsinised and washed twice in PBS before pellets were transferred to

766 microcentrifuge tubes and snap-frozen. Pellets were resuspended in 200µl deionised

767 water, sonicated for 20 seconds using an ultrasonic processor (Sonics & Materials

768 Inc., CT, USA), then placed on ice. 750 µl of isopropanol containing 4 µmol/L 5α-

769 cholestane as an internal standard was added to each sample, and then each was

770 sonicated for a further 10 seconds. Lysates were transferred to 7ml glass vials and

771 mixed with 250 µl tetramethylammonium hydroxide for alkalyine saponification at

772 80°C for 15 min, then cooled down for 10 minutes at room temperature. Sterols were

773 extracted by addition of 500 µl tetrachloroethylene/methyl butyrate (1:3) and 2 ml

774 deionised water, then thorough mixing. Samples were centrifuged for 10 minutes at

775 3000 rpm, and the organic phase containing the sterols was transferred to 300 µl GC

776 vials. Extracts were dried under a stream of nitrogen, then sterols were silylated with

777 50 µL Tri-Sil HTP (HDMS:TMCS:Pyridine) Reagent (ThermoFisher) at 60°C for 1

778 hour.

779 Chromatography separation was performed on an Agilent gas chromatography-mass

780 spectrometry (GC-MS) system (6890A GC and 5973 MS) (Agilent Technologies,

781 Inc., CA, USA) with an HP-1MS capillary column (30 m length. x 250 µm diameter x

782 0.25 µm film thickness). The GC temperature gradient was as follows: Initial

783 temperature of 120°C increased to 200°C at a rate of 20°C/min, then increased to

784 300°C at a rate of 2°C/min with a 15 minute solvent delay. Injection was at 250°C in

785 splitless mode with ultrapurified helium as the carrier gas and the transfer line was

786 280°C. The mass spectra were acquired by electron impact at 70 eV using selected

787 ion monitoring as follows: Lathosterol-TMS, cholesterol-TMS, and cholest8(9)-enol-

788 TMS: m/z 458; 5α-cholestane and desmosterol-TMS: m/z 372; Lanosterol-TMS: m/z

789 393; and 7-dehydrocholesterol-TMS: m/z 325. The data were analysed using

790 MassHunter Workstation Quantitative Analysis Software (Agilent Technologies, Inc.)

791 and OriginPro 2017 (OriginLab Corp, MA, USA).

792

793 <u>Molecular dynamics</u>

794 Simulations were constructed as previously described, starting from a modified

795 version of the OSBPL2 lipid-binding domain structure (PDB 5ZM8)(Wang et al.,

796 2019). Parameters for lathosterol were obtained by modifying those of cholesterol to

797 substituting the double bond between C5-C6 with one between C7-C8. Simulations

798 were performed with the CHARMM36 force field.

799

800 <u>Western blotting</u>

801 Cell lysates were made with a buffer containing 150mM NaCl, 0.5% Triton-X-100

802 and EDTA-free protease-inhibitor solution (Expedeon), 50mM Tris, pH=7.4. Cell

803 lysates and input samples from BioID and immunoprecipitation experiments were

804 combined 1:1 with a 2x reducing loading buffer; a reducing loading buffer containing

805 10mM EDTA was added directly to Dynabead samples. SDS–PAGE and Western

806 blotting were carried out according to standard methods.

807

808 ACKNOWLEDGEMENTS

809 We thank the Warburg Micro syndrome children and their families. We thank

810 Professor C. A. Johnson and Dr J. A. Poulter for a critical reading of the manuscript.

811

812 COMPETING INTERESTS

813 No competing interests declared.

814

815 FUNDING

816 MH is supported by the University of Leeds and by a Programme Grant from the

817 Newlife Foundation for Disabled Children (Grant Reference Number: 17-18/23).

818

819 DATA AVAILABILITY

820   The mass spectrometry proteomics data have been deposited to the

821   ProteomeXchange Consortium via the PRIDE (Perez-Riverol et al., 2019) partner

822   repository with the dataset identifiers PXD016631, PXD016336, PXD016326,

823   PXD016233 and PXD016404.

824   REFERENCES

825

826   Aligianis IA, Johnson CA, Gissen P, Chen D, Hampshire D, Hoffmann K, Maina EN,
827   Morgan NV, Tee L, Morton J, Ainsworth JR, Horn D, Rosser E, Cole TR, Stolte-
828   Dijkstra I, Fieggen K, Clayton-Smith J, Megarbane A, Shield JP, Newbury-Ecob R et
829   al. (2005) Mutations of the catalytic subunit of RAB3GAP cause Warburg Micro
830   syndrome. *Nat Genet* 37: 221-3

831   Anderson R, Rust S, Ashworth J, Clayton-Smith J, Taylor RL, Clayton PT, Morris
832   AAM (2019) Lathosterolosis: A Relatively Mild Case with Cataracts and Learning
833   Difficulties. *JIMD Rep* 44: 79-84

834   Antonny B, Bigay J, Mesmin B (2018) The Oxysterol-Binding Protein Cycle: Burning
835   Off PI(4)P to Transport Cholesterol. *Annu Rev Biochem* 87: 809-837

836   Barr F, Lambright DG (2010) Rab GEFs and GAPs. *Curr Opin Cell Biol* 22: 461-70

837   Bekbulat F, Schmitt D, Feldmann A, Huesmann H, Eimer S, Juretschke T, Beli P,
838   Behl C, Kern A (2019) RAB18 Loss Interferes With Lipid Droplet Catabolism and
839   Provokes Autophagy Network Adaptations. *J Mol Biol* 432: 1216-34

840   Bem D, Yoshimura S, Nunes-Bastos R, Bond FC, Kurian MA, Rahman F, Handley
841   MT, Hadzhiev Y, Masood I, Straatman-Iwanowska AA, Cullinane AR, McNeill A,
842   Pasha SS, Kirby GA, Foster K, Ahmed Z, Morton JE, Williams D, Graham JM,
843   Dobyns WB et al. (2011) Loss-of-function mutations in RAB18 cause Warburg micro
844   syndrome. *Am J Hum Genet* 88: 499-507

845   Borck G, Wunram H, Steiert A, Volk AE, Korber F, Roters S, Herkenrath P, Wollnik
846   B, Morris-Rosendahl DJ, Kubisch C (2011) A homozygous RAB3GAP2 mutation
847   causes Warburg Micro syndrome. *Human genetics* 129: 45-50

848   Branon TC, Bosch JA, Sanchez AD, Udeshi ND, Svinkina T, Carr SA, Feldman JL,
849   Perrimon N, Ting AY (2018) Efficient proximity labeling in living cells and organisms
850   with TurboID. *Nat Biotechnol* 36: 880-887

851   Brunet S, Saint-Dic D, Milev MP, Nilsson T, Sacher M (2016) The TRAPP Subunit
852   Trs130p Interacts with the GAP Gyp6p to Mediate Ypt6p Dynamics at the Late Golgi.
853   *Front Cell Dev Biol* 4: 48

854   Brunetti-Pierri N, Corso G, Rossi M, Ferrari P, Balli F, Rivasi F, Annunziata I,
855   Ballabio A, Russo AD, Andria G, Parenti G (2002) Lathosterolosis, a novel multiple-
856   malformation/mental retardation syndrome due to deficiency of 3beta-
857   hydroxysteroid-delta5-desaturase. *Am J Hum Genet* 71: 952-8

858   Carney DS, Davies BA, Horazdovsky BF (2006) Vps9 domain-containing proteins:
859   activators of Rab5 GTPases from yeast to neurons. *Trends Cell Biol* 16: 27-35

860   Carpanini SM, McKie L, Thomson D, Wright AK, Gordon SL, Roche SL, Handley MT,
861   Morrison H, Brownstein D, Wishart TM, Cousin MA, Gillingwater TH, Aligianis IA,
862   Jackson IJ (2014) A novel mouse model of Warburg Micro syndrome reveals roles
863   for RAB18 in eye development and organisation of the neuronal cytoskeleton.
864   *Disease models & mechanisms* 7: 711-22

865   Christoforidis S, McBride HM, Burgoyne RD, Zerial M (1999) The Rab5 effector
866   EEA1 is a core component of endosome docking. *Nature* 397: 621-5

867 Correa-Cerro LS, Wassif CA, Kratz L, Miller GF, Munasinghe JP, Grinberg A, Fliesler
868 SJ, Porter FD (2006) Development and characterization of a hypomorphic Smith-
869 Lemli-Opitz syndrome mouse model and efficacy of simvastatin therapy. *Hum Mol*
870 *Genet* 15: 839-51

871 Cox J, Hein MY, Luber CA, Paron I, Nagaraj N, Mann M (2014) Accurate proteome-
872 wide label-free quantification by delayed normalization and maximal peptide ratio
873 extraction, termed MaxLFQ. *Mol Cell Proteomics* 13: 2513-26

874 Fliesler SJ, Peachey NS, Herron J, Hines KM, Weinstock NI, Ramachandra Rao S,
875 Xu L (2018) Prevention of Retinal Degeneration in a Rat Model of Smith-Lemli-Opitz
876 Syndrome. *Sci Rep* 8: 1286

877 Fukuda M, Kanno E, Ishibashi K, Itoh T (2008) Large scale screening for novel rab
878 effectors reveals unexpected broad Rab binding specificity. *Mol Cell Proteomics* 7:
879 1031-42

880 Gerondopoulos A, Bastos RN, Yoshimura S, Anderson R, Carpanini S, Aligianis I,
881 Handley MT, Barr FA (2014) Rab18 and a Rab18 GEF complex are required for
882 normal ER structure. *The Journal of cell biology* 205: 707-20

883 Gillingham AK, Bertram J, Begum F, Munro S (2019) In vivo identification of GTPase
884 interactors by mitochondrial relocalization and proximity biotinylation. *Elife* 8: e45916

885 Gillingham AK, Sinka R, Torres IL, Lilley KS, Munro S (2014) Toward a
886 comprehensive map of the effectors of rab GTPases. *Developmental cell* 31: 358-73

887 Handley M, Sheridan E (2018) RAB18 Deficiency. In *GeneReviews*((R)), Adam MP,
888 Ardinger HH, Pagon RA, Wallace SE, Bean LJH, Stephens K, Amemiya A (eds)
889 Seattle (WA): NBK475670

890 Handley MT, Carpanini SM, Mali GR, Sidjanin DJ, Aligianis IA, Jackson IJ,
891 FitzPatrick DR (2015) Warburg Micro syndrome is caused by RAB18 deficiency or
892 dysregulation. *Open biology* 5: 150047

893 Hendershott MC, Vale RD (2014) Regulation of microtubule minus-end dynamics by
894 CAMSAPs and Patronin. *Proc Natl Acad Sci U S A* 111: 5860-5

895 Ho AC, Fung CW, Siu TS, Ma OC, Lam CW, Tam S, Wong VC (2014)
896 Lathosterolosis: a disorder of cholesterol biosynthesis resembling smith-lemli-opitz
897 syndrome. *JIMD Rep* 12: 129-34

898 Hueschen CL, Kenny SJ, Xu K, Dumont S (2017) NuMA recruits dynein activity to
899 microtubule minus-ends at mitosis. *Elife* 6: e29328

900 Im YJ, Raychaudhuri S, Prinz WA, Hurley JH (2005) Structural mechanism for sterol
901 sensing and transport by OSBP-related proteins. *Nature* 437: 154-8

902 Jin J, Sison K, Li C, Tian R, Wnuk M, Sung HK, Jeansson M, Zhang C, Tucholska M,
903 Jones N, Kerjaschki D, Shibuya M, Fantus IG, Nagy A, Gerber HP, Ferrara N,
904 Pawson T, Quaggin SE (2012) Soluble FLT1 binds lipid microdomains in podocytes
905 to control cell morphology and glomerular barrier function. *Cell* 151: 384-99

906 Jira P, Wevers R, de Jong J, Rubio-Gozalbo E, Smeitink J (1997) New treatment
907 strategy for Smith-Lemli-Opitz syndrome. *The Lancet* 349: 1222

908 Kim DI, Jensen SC, Noble KA, Kc B, Roux KH, Motamedchaboki K, Roux KJ (2016)
909 An improved smaller biotin ligase for BioID proximity labeling. *Mol Biol Cell* 27: 1188-
910 96

911 Korade Z, Xu L, Harrison FE, Ahsen R, Hart SE, Folkes OM, Mirnics K, Porter NA
912 (2014) Antioxidant supplementation ameliorates molecular deficits in Smith-Lemli-
913 Opitz syndrome. *Biol Psychiatry* 75: 215-22

914 Krakowiak PA, Wassif CA, Kratz L, Cozma D, Kovarova M, Harris G, Grinberg A,
915 Yang Y, Hunter AG, Tsokos M, Kelley RI, Porter FD (2003) Lathosterolosis: an
916 inborn error of human and murine cholesterol synthesis due to lathosterol 5-
917 desaturase deficiency. *Hum Mol Genet* 12: 1631-41

918 Kumar D, Golchoubian B, Belevich I, Jokitalo E, Schlaitz AL (2019) REEP3 and
919 REEP4 determine the tubular morphology of the endoplasmic reticulum during
920 mitosis. *Mol Biol Cell* 30: 1377-1389

921 Lamber EP, Siedenburg AC, Barr FA (2019) Rab regulation by GEFs and GAPs
922 during membrane traffic. *Curr Opin Cell Biol* 59: 34-39

923 Lees JA, Messa M, Sun EW, Wheeler H, Torta F, Wenk MR, De Camilli P, Reinisch
924 KM (2017) Lipid transport by TMEM24 at ER-plasma membrane contacts regulates
925 pulsatile insulin secretion. *Science* 355: eaah6171

926 Levin-Konigsberg R, Montaño-Rendón F, Keren-Kaplan T, Li R, Ego B, Mylvaganam
927 S, DiCiccio JE, Trimble WS, Bassik MC, Bonifacino JS, Fairn GD, Grinstein S (2019)
928 Phagolysosome resolution requires contacts with the endoplasmic reticulum and
929 phosphatidylinositol-4-phosphate signalling. *Nat Cell Biol* 20: 1234-47

930 Li C, Luo X, Zhao S, Siu GK, Liang Y, Chan HC, Satoh A, Yu SS (2017) COPI-
931 TRAPPII activates Rab18 and regulates its lipid droplet association. *EMBO J* 36:
932 441-457

933 Li D, Zhao YG, Li D, Zhao H, Huang J, Miao G, Feng D, Liu P, Li D, Zhang H (2019)
934 The ER-Localized Protein DFCP1 Modulates ER-Lipid Droplet Contact Formation.
935 *Cell Rep* 27: 343-358 e5

936 Liegel RP, Handley MT, Ronchetti A, Brown S, Langemeyer L, Linford A, Chang B,
937 Morris-Rosendahl DJ, Carpanini S, Posmyk R, Harthill V, Sheridan E, Abdel-Salam
938 GM, Terhal PA, Faravelli F, Accorsi P, Giordano L, Pinelli L, Hartmann B, Ebert AD
939 et al. (2013) Loss-of-function mutations in TBC1D20 cause cataracts and male
940 infertility in blind sterile mice and Warburg micro syndrome in humans. *Am J Hum*
941 *Genet* 93: 1001-14

942 Lind GE, Raiborg C, Danielsen SA, Rognum TO, Thiis-Evensen E, Hoff G,
943 Nesbakken A, Stenmark H, Lothe RA (2011) SPG20, a novel biomarker for early
944 detection of colorectal cancer, encodes a regulator of cytokinesis. *Oncogene* 30:
945 3967-78

946 Liu X, Salokas K, Tamene F, Jiu Y, Weldatsadik RG, Ohman T, Varjosalo M (2018)
947 An AP-MS- and BioID-compatible MAC-tag enables comprehensive mapping of
948 protein interactions and subcellular localizations. *Nat Commun* 9: 1188

949 Nakamura H, Yamashita N, Kimura A, Kimura Y, Hirano H, Makihara H, Kawamoto
950 Y, Jitsuki-Takahashi A, Yonezaki K, Takase K, Miyazaki T, Nakamura F, Tanaka F,
951 Goshima Y (2016) Comprehensive behavioral study and proteomic analyses of
952 CRMP2-deficient mice. *Genes Cells* 21: 1059-1079

953 Ng BG, Lourenço CM, Losfeld ME, Buckingham KJ, Kircher M, Nickerson DA,
954 Shendure J, Bamshad MJ; University of Washington Center for Mendelian
955 Genomics, Freeze HH (2019) Mutations in the translocon-associated protein

956 complex subunit SSR3 cause a novel congenital disorder of glycosylation. *J Inherit*
957 *Metab Dis* 42: 993-7

958 Nicholson JM, Macedo JC, Mattingly AJ, Wangsa D, Camps J, Lima V, Gomes AM,
959 Doria S, Ried T, Logarinho E, Cimini D (2015) Chromosome mis-segregation and
960 cytokinesis failure in trisomic human cells. *Elife* 4: e05068

961 Nowaczyk MJM, Wassif CA (1998) Smith-Lemli-Opitz Syndrome. In
962 *GeneReviews*((R)), Adam MP, Ardinger HH, Pagon RA, Wallace SE, Bean LJH,
963 Stephens K, Amemiya A (eds) Seattle (WA): NBK1143

964 Ong WY, Ng MP, Loke SY, Jin S, Wu YJ, Tanaka K, Wong PT (2013)
965 Comprehensive gene expression profiling reveals synergistic functional networks in
966 cerebral vessels after hypertension or hypercholesterolemia. *PloS one* 8: e68335

967 Perez-Riverol Y, Csordas A, Bai J, Bernal-Llinares M, Hewapathirana S, Kundu DJ,
968 Inuganti A, Griss J, Mayer G, Eisenacher M, Perez E, Uszkoreit J, Pfeuffer J,
969 Sachsenberg T, Yilmaz S, Tiwary S, Cox J, Audain E, Walzer M, Jarnuczak AF et al.
970 (2019) The PRIDE database and related tools and resources in 2019: improving
971 support for quantification data. *Nucleic Acids Res* 47: D442-D450

972 Platt FM, Wassif C, Colaco A, Dardis A, Lloyd-Evans E, Bembi B, Porter FD (2014)
973 Disorders of cholesterol metabolism and their unanticipated convergent mechanisms
974 of disease. *Annu Rev Genomics Hum Genet* 15: 173-94

975 Ran FA, Hsu PD, Wright J, Agarwala V, Scott DA, Zhang F (2013) Genome
976 engineering using the CRISPR-Cas9 system. *Nat Protoc* 8: 2281-2308

977 Ren Y, Yip CK, Tripathi A, Huie D, Jeffrey PD, Walz T, Hughson FM (2009) A
978 structure-based mechanism for vesicle capture by the multisubunit tethering complex
979 Dsl1. *Cell* 139: 1119-29

980 Richter KN, Revelo NH, Seitz KJ, Helm MS, Sarkar D, Saleeb RS, D'Este E, Eberle
981 J, Wagner E, Vogl C, Lazaro DF, Richter F, Coy-Vergara J, Coceano G, Boyden ES,
982 Duncan RR, Hell SW, Lauterbach MA, Lehnart SE, Moser T et al. (2018) Glyoxal as
983 an alternative fixative to formaldehyde in immunostaining and super-resolution
984 microscopy. *EMBO J* 37: 139-159

985 Rocha N, Kuijl C, van der Kant R, Janssen L, Houben D, Janssen H, Zwart W,
986 Neefjes J (2009) Cholesterol sensor ORP1L contacts the ER protein VAP to control
987 Rab7-RILP-p150 Glued and late endosome positioning. *The Journal of cell biology*
988 185: 1209-25

989 Rossi M, D'Armiento M, Parisi I, Ferrari P, Hall CM, Cervasio M, Rivasi F, Balli F,
990 Vecchione R, Corso G, Andria G, Parenti G (2007) Clinical phenotype of
991 lathosterolosis. *Am J Med Genet A* 143A: 2371-81

992 Rossi V, Banfield DK, Vacca M, Dietrich LE, Ungermann C, D'Esposito M, Galli T,
993 Filippini F (2004) Longins and their longin domains: regulated SNAREs and
994 multifunctional SNARE regulators. *Trends Biochem Sci* 29: 682-8

995 Roux KJ, Kim DI, Burke B, May DG (2018) BioID: A Screen for Protein-Protein
996 Interactions. *Curr Protoc Protein Sci* 91: 19.23.1-19.23.15

997 Roux KJ, Kim DI, Raida M, Burke B (2012) A promiscuous biotin ligase fusion
998 protein identifies proximal and interacting proteins in mammalian cells. *The Journal*
999 *of cell biology* 196: 801-10

1000   Schlaitz AL, Thompson J, Wong CC, Yates JR, 3rd, Heald R (2013) REEP3/4
1001   ensure endoplasmic reticulum clearance from metaphase chromatin and proper
1002   nuclear envelope architecture. *Developmental cell* 26: 315-23

1003   Silve S, Dupuy PH, Labit-Lebouteiller C, Kaghad M, Chalon P, Rahier A, Taton M,
1004   Lupker J, Shire D, Loison G (1996) Emopamil-binding protein, a mammalian protein
1005   that binds a series of structurally diverse neuroprotective agents, exhibits delta8-
1006   delta7 sterol isomerase activity in yeast. *The Journal of biological chemistry* 271:
1007   22434-40

1008   Sobajima T, Yoshimura SI, Maeda T, Miyata H, Miyoshi E, Harada A (2018) The
1009   Rab11-binding protein RELCH/KIAA1468 controls intracellular cholesterol
1010   distribution. *The Journal of cell biology* 217: 1777-1796

1011   Spang A (2012) The DSL1 complex: the smallest but not the least CATCHR. *Traffic*
1012   13: 908-13

1013   Svoboda MD, Christie JM, Eroglu Y, Freeman KA, Steiner RD (2012) Treatment of
1014   Smith-Lemli-Opitz syndrome and other sterol disorders. *Am J Med Genet C Semin*
1015   *Med Genet* 160C: 285-94

1016   Tinti M, Johnson C, Toth R, Ferrier DE, Mackintosh C (2012) Evolution of signal
1017   multiplexing by 14-3-3-binding 2R-ohnologue protein families in the vertebrates.
1018   *Open biology* 2: 120103

1019   Urnavicius L, Zhang K, Diamant AG, Motz C, Schlager MA, Yu M, Patel NA,
1020   Robinson CV, Carter AP (2015) The structure of the dynactin complex and its
1021   interaction with dynein. *Science* 347: 1441-1446

1022   Wang H, Ma Q, Qi Y, Dong J, Du X, Rae J, Wang J, Wu WF, Brown AJ, Parton RG,
1023   Wu JW, Yang H (2019) ORP2 Delivers Cholesterol to the Plasma Membrane in
1024   Exchange for Phosphatidylinositol 4, 5-Bisphosphate (PI(4,5)P2). *Mol Cell* 73: 458-
1025   473 e7

1026   Wassif CA, Kratz L, Sparks SE, Wheeler C, Bianconi S, Gropman A, Calis KA,
1027   Kelley RI, Tierney E, Porter FD (2017) A placebo-controlled trial of simvastatin
1028   therapy in Smith-Lemli-Opitz syndrome. *Genet Med* 19: 297-305

1029   Whitfield ST, Burston HE, Bean BD, Raghuram N, Maldonado-Baez L, Davey M,
1030   Wendland B, Conibear E (2016) The alternate AP-1 adaptor subunit Apm2 interacts
1031   with the Mil1 regulatory protein and confers differential cargo sorting. *Mol Biol Cell*
1032   27: 588-98

1033   Williams C, Choudhury R, McKenzie E, Lowe M (2007) Targeting of the type II
1034   inositol polyphosphate 5-phosphatase INPP5B to the early secretory pathway. *J Cell*
1035   *Sci* 120: 3941-51

1036   Xu D, Li Y, Wu L, Li Y, Zhao D, Yu J, Huang T, Ferguson C, Parton RG, Yang H, Li
1037   P (2018) Rab18 promotes lipid droplet (LD) growth by tethering the ER to LDs
1038   through SNARE and NRZ interactions. *The Journal of cell biology* 217: 975-995

1039   Yamaguchi T, Dulubova I, Min SW, Chen X, Rizo J, Südhof TC (2002) Sly1 binds to
1040   Golgi and ER syntaxins via a conserved N-terminal peptide motif. *Dev Cell* 2: 295-
1041   305

1042   Zhao L, Imperiale MJ (2017) Identification of Rab18 as an Essential Host Factor for
1043   BK Polyomavirus Infection Using a Whole-Genome RNA Interference Screen.
1044   *mSphere* 2: e00291-17

1045   Zhen Y, Stenmark H (2015) Cellular functions of Rab GTPases at a glance. *J Cell*
1046   *Sci* 128: 3171-6
1047
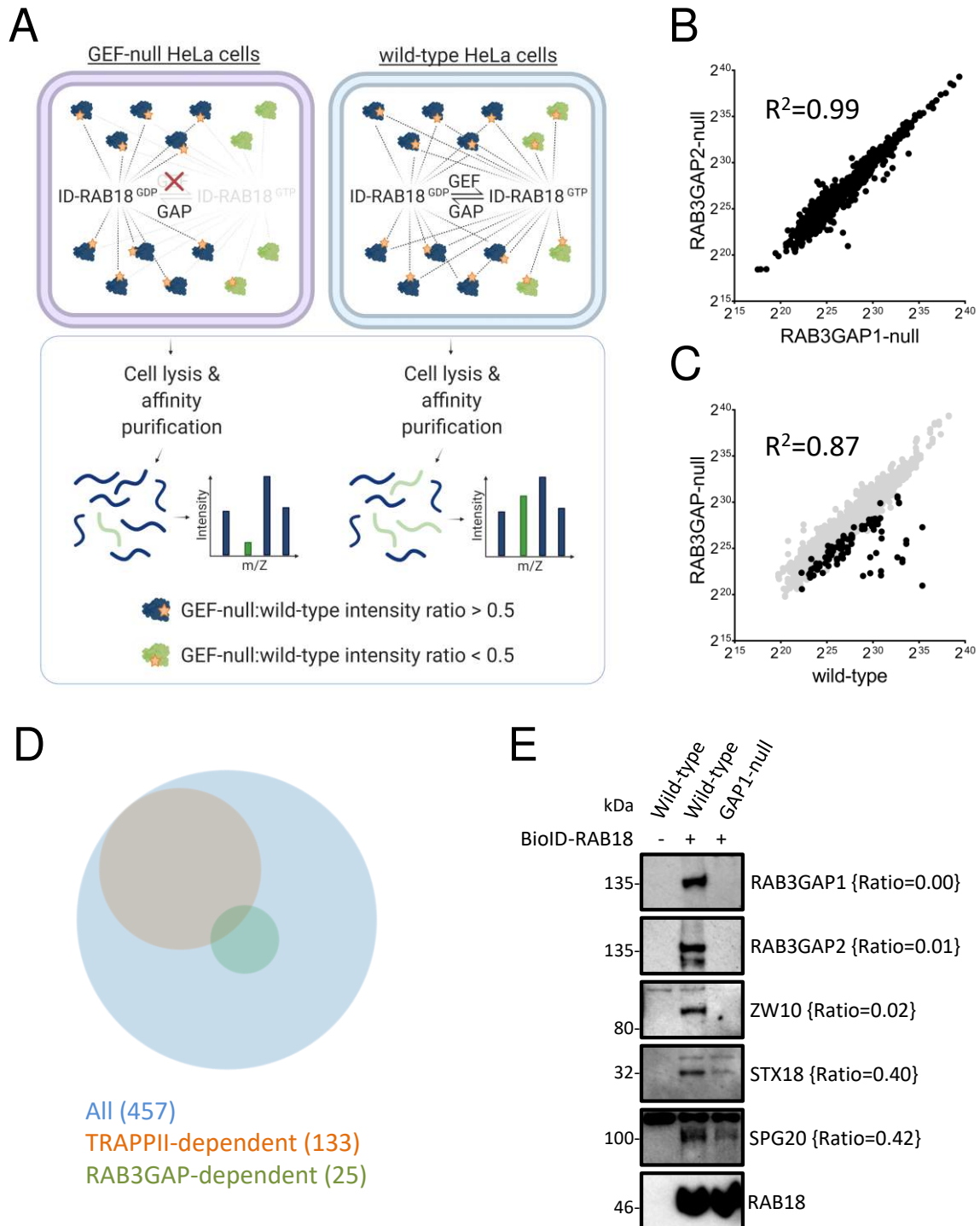
Figure 1. RAB3GAP-dependent RAB18-interactions in HeLa cells. (A) Schematic to show experimental approach. Proximity biotinylation of guanine nucleotide exchange factor (GEF)-dependent interactors by BirA*-RAB18 (ID-RAB18) is disrupted in GEF-null cells. GEF-independent interactors are biotinylated in both GEF-null and wild-type cells. Following affinity purification, GEF-dependent

1055   interactions are determined by LFQ intensity ratios. (B) Plot to show correlation

1056   between Log_2 LFQ intensities of individual proteins identified in samples purified

1057   from RAB3GAP1- and RAB3GAP2-null cells. (C) Plot to show correlation between

1058 Log_2 LFQ intensities of individual proteins identified in samples purified from wild-

1059   type and RAB3GAP-null cells. Highlighted datapoints correspond to proteins later

1060   found to have RAB3GAP-null:wild-type intensity ratios <0.5. (D) Venn diagram to

1061   show overlap between all RAB18-associations, TRAPPII-dependent interactions

1062   (TRAPPC9-null:wild-type intensity ratios <0.5) and RAB3GAP-dependent

1063   associations (RAB3GAP-null:wild-type intensity ratios <0.5). (E) Western blotting of

1064   samples purified from wild-type and RAB3GAP1-null cells in an independent BioID

1065   experiment. Levels of selected proteins are consistent with RAB3GAP-null:wild-type

1066   intensity ratios {braces}.

1067

1068

1069

Protein	n	Ratio	Orthologue PPI (Gillingham et al., 2014)	Additional evidence	
CAMSAP1	3	0.26			Microtubule/membrane remodelling
REEP4	3	0.35		Tinti et al., 2012*	
BICD2	2	0.25	BicD	Gillingham et al., 2019	
SPG20	**2**	**0.42**	**CG12001**	**This study (Figure 2)**	
ZW10	3	0.02	mit(1)15	Xu et al., 2018; Gillingham et al., 2019	Membrane tethering/docking
RINT1	3	0.16	CG8605	Xu et al., 2018	
NBAS	3	0.17	rod	Xu et al., 2018; Gillingham et al., 2019	
SCFD2	3	0.41	Slh	Gillingham et al., 2019	
SEC22A	**3**	**0.46**		**This study (Figure 3)**	
BNIP1	2	0.36		Xu et al., 2018	
STX18	2	0.40	Syx18	Xu et al., 2018	
TMCO4	**3**	**0.06**		**This study (Figure 4)**	Lipid modifying/ mobilising
OSBPL2	**3**	**0.35**		**This study (Figure 5)**	
EBP	**3**	**0.38**		**This study (Figure 5)**	
INPP5B	**2**	**0.00**		**This study (Figure 5)**	
C2CD2L	2	0.22			
C2CD2	2	0.36			
TRIM13	2	0.29			Autophagy receptors
FAM134B	2	0.46			
RAB3GAP2	3	0.00	rab3-GAP	Gerondopoulos et al., 2014	Other
RAB3GAP1	3	0.01	CG31935	Gerondopoulos et al., 2014	
SSR3	3	0.49			
MFHAS1	2	0.00	lrrk		
WFS1	2	0.00			
SCARA3	2	0.42			

1070
1071 **Table 1. RAB3GAP-dependent RAB18-interactions in HeLa cells.** 25 proteins

1072 with mean RAB3GAP-null:wild-type intensity ratios <0.5, identified in two or more

1073 independent proximity biotinylation experiments. Orthologous proteins identified by

1074 Gillingham et al., 2014, and other studies providing supporting evidence for

1075 interactions are shown. Proteins are grouped according to their reported functions.

1076 The full dataset is provided in Table S1.

Gene(s)	Homologue(s)	Syndrome(s)	Inheritance	OMIM	Overlapping features
RAB3GAP1, RAB3GAP2, RAB18, TBC1D20	-	Warburg Micro syndrome; Martsolf syndrome	AR	600118, 614222, 614225, 615663; 212720	intellectual disability (ID), microcephaly (M), ascending spastic paraplegia (ASP), cataract (C), microphthalmia (Mo), microcornea (Mc), optic atrophy (OA), seizures (S), corpus callosum hypogenesis (CCH), cerebellar vermis hypoplasia (CVH), genital abnormalities (GA), Neuropathy (N)
EBP	-	CDPX2; MEND syndrome	XLD; XLR	302960; 300960	ID, M, C, Mo, Mc, S, CCH, CVH, GA
INPP5B	*OCRL*; *INPP5K*	Lowe syndrome; MDCCAID	XLR; AR	309000; 607875	ID, M, C, S
SSR3	-	Congenital disorder of glycosylation	AR	Ng et al., 2019	ID, M, CCH, GA
WFS1	-	Wolfram syndrome; CTRCT41	AR; AD	222300; 116400	C, OA, GA
SPG20	-	Troyer syndrome (SPG20)	AR	275900	ID, M, ASP
BICD2	-	Spinal muscular atrophy	AD	615290; 615291	ASP
REEP4	*REEP1*; *REEP2*	SPG31; SPG72	AD	610250; 615625	ASP
NBAS	-	SOPH syndrome	AR	614800	OA
FAM134B	-	HSAN IIB	AR	613115	N

Table 2. Genes encoding putative RAB18 effectors or their homologues are associated with diseases that share overlapping features with Warburg Micro syndrome. AR, autosomal recessive; XLD, X-linked dominant; XLR, X-linked recessive; AD, autosomal dominant.
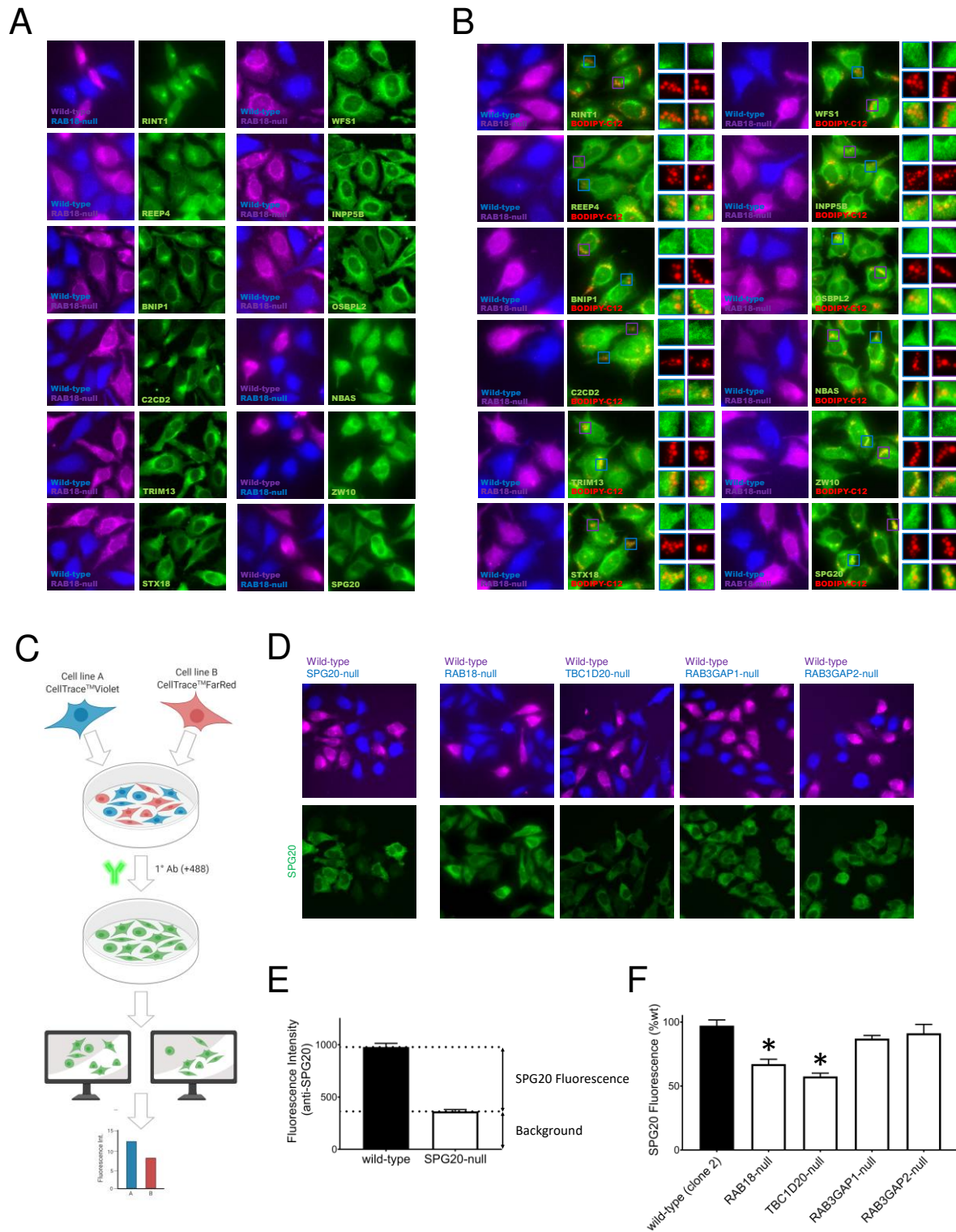
1084

1085

1086 **Figure 2. Initial screening of putative RAB18 effectors reveals that levels of**

1087 **SPG20 are significantly reduced in RAB18-null and TBC1D20-null cells.** (A)

1088 Comparative fluorescence microscopy of selected RAB18-associated proteins in

1089 wild-type and RAB18-null HeLa cells. Cells of different genotypes were labelled with

41

1090   CellTrace-Violet and CellTrace-Far Red reagents, corresponding to blue and

1091   magenta channels respectively. Cells were stained with antibodies against indicated

1092   proteins in green channel panels. (B) Comparative fluorescence microscopy of

1093   selected RAB18-associated proteins in lipid-loaded wild-type and RAB18-null HeLa

1094   cells. Cells were stained as above but were treated for 15 hours with 200µM oleic

1095   acid, 1µg/ml BODIPY-558/568-C12 (Red channel) prior to fixation. (C) Schematic to

1096   show method for quantification of protein levels by fluorescence intensity. In each

1097   frame, cell areas for each genotype are generated by thresholding CellTrace

1098   channels, intensity of antibody-staining is measured for each cell in multiple frames.

1099   (D) Example frames showing wild-type and mutant cells of the indicated genotypes,

1100   labelled with CellTrace-Far Red and CellTrace-Violet and reagents respectively, then

1101   stained for SPG20. (E) Quantification of SPG20-specific fluorescence in wild-type

1102   cells by direct comparison with SPG20-null cells. (F) Quantification of SPG20

1103   fluorescence (%wt) in cells of different genotypes. Data were derived from analysis

1104   of at least 18 frames – each containing >5 wild-type and >5 mutant cells – per

1105   genotype. Error bars represent s.e.m. *p<0.001.

1106
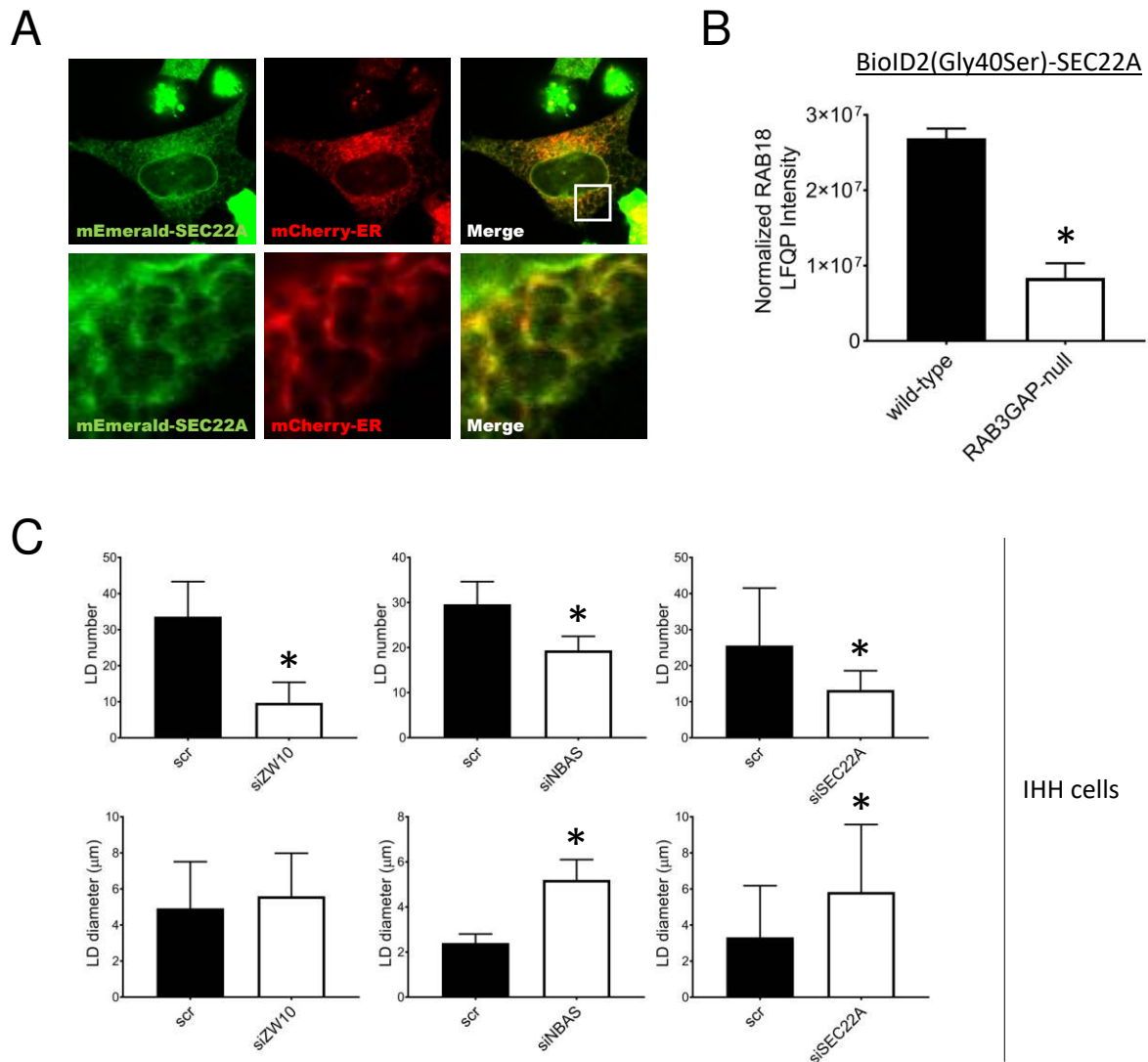
Figure 3. SEC22A associates with RAB18 and influences LD morphology. (A) Confocal micrograph to show overlapping localization of exogenous mEmerald-SEC22A (Green) and mCherry-ER (Red) in HeLa cells. (B) RAB18 LFQ intensities from a reciprocal BioID experiment showing a reduced association between BioID2(Gly40Ser)-SEC22A and endogenous RAB18 in RAB3GAP-null compared to wild-type HeLa cells. Data were adjusted to account for non-specific binding of RAB18 to beads and normalized by SEC22A LFQ intensities in each replicate experiment. Error bars represent s.e.m. Data for other BioID2(Gly40Ser)-SEC22A-associated proteins are provided in table S5. (C) Bar graphs to show effects of ZW10, NBAS and SEC22A knockdowns on lipid droplet number and diameter. siRNA-treated IHH cells were loaded with 200nM BSA-conjugated oleate, fixed and stained with BODIPY and DAPI, and imaged. Images were analysed using ImageJ.

43

1120   Data are derived from measurements from >100 cells/condition and are

1121   representative of three independent experiments. Error bars represent SD. *$p < 0.001$

1122
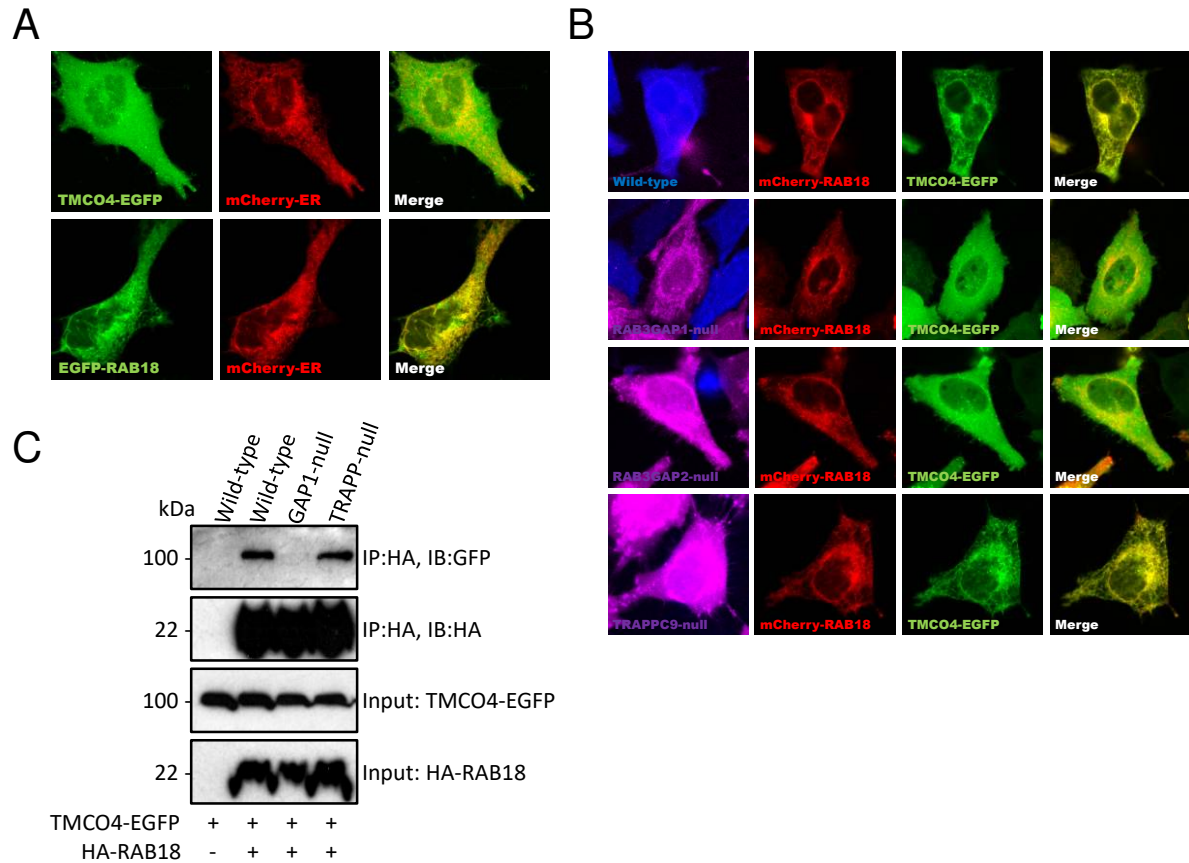
Figure 4. mCherry-RAB18 recruits TMCO4-EGFP to the ER membrane in a RAB3GAP-dependent manner. (A) Confocal micrographs to show diffuse localization of exogenous TMCO4-EGFP (Green) compared to mCherry-ER (Red) and overlapping localization of exogenous EGFP-RAB18 (Green) and mCherry-ER in HeLa cells. (B) Confocal micrographs to show localization of exogenous mCherry-RAB18 and TMCO4-EGFP in wild-type cells and in mutant cells of different genotypes. Wild-type and mutant cells of the indicated genotypes were labelled with CellTrace-Violet and CellTrace-Far Red reagents respectively (magenta and blue channels). (C) Immunoprecipitation of exogenous HA-RAB18 from HeLa cells of different genotypes. Cells were transfected with the indicated constructs and lysed 24 hours post-transfection. Anti-HA immunoprecipitates and input samples were subjected to SDS-PAGE and immunostaining for HA and GFP.

45
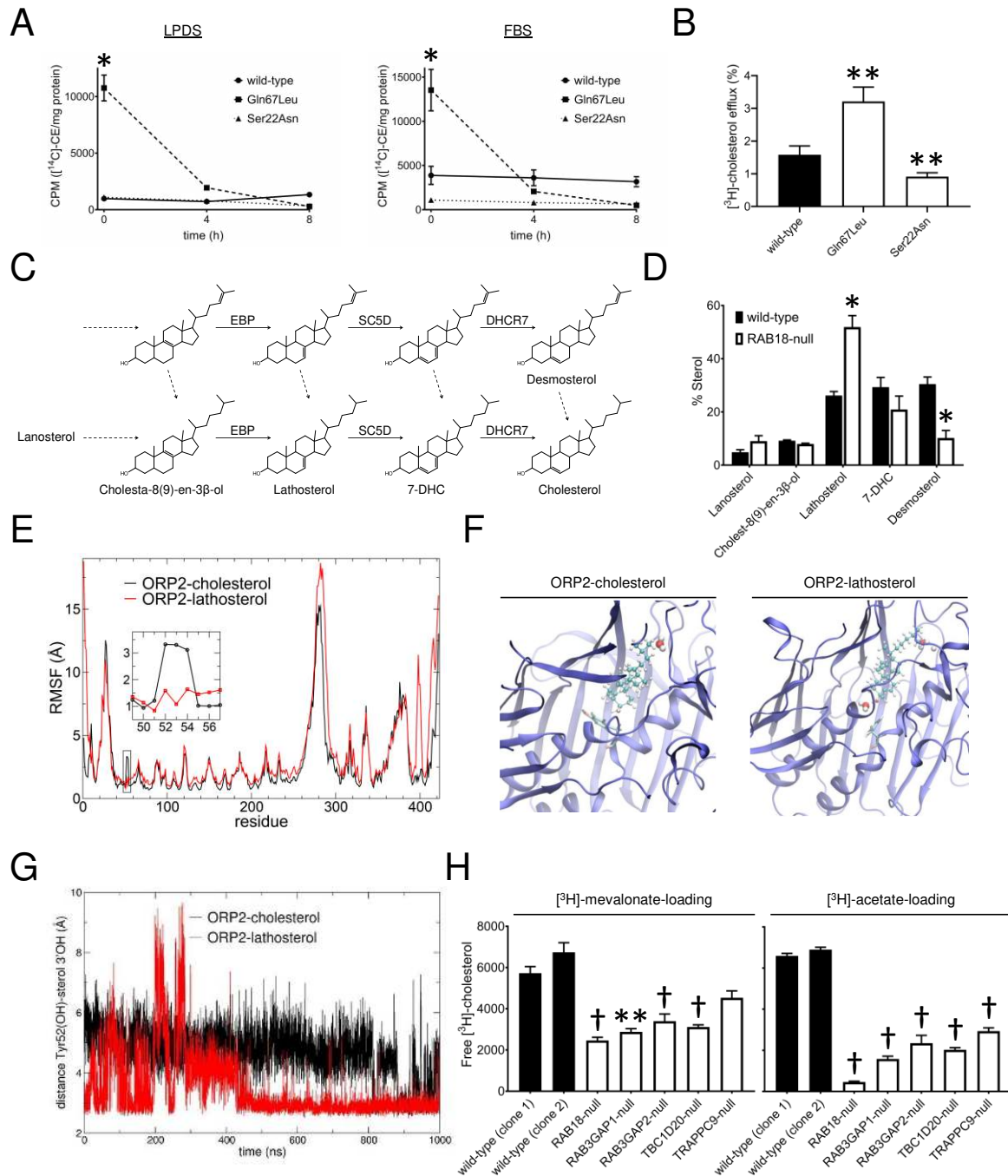
Figure 5. RAB18 is involved in the mobilization and biosynthesis of cholesterol. (A) Plots to show cholesteryl ester (CE) loading and efflux. CHO cells, stably expressing RAB18(WT), RAB18(Gln67Leu) and RAB18(Ser22Asn), were incubated with [^{14}C]-oleate, for 24 hours, in the presence of lipoprotein depleted serum (LPDS)(Left panel) or FBS (Right panel). Following lipid extraction, thin layer chromatography (TLC) was used to separate CE, and radioactivity was measured by scintillation counting. Measurements were made at t=0 and at 4 and 8 hours

46

1146   following the addition of 50μg/ml high density lipoprotein (HDL) to the cells. (B) Bar

1147   graph to show cholesterol efflux. CHO cells were incubated with [^{3}H]-cholesterol, for

1148   24 hours, in the presence of FBS. After washing, they were incubated with 25μg/ml

1149   apolipoprotein A-I for 5 hours. The quantity of [^{3}H]-cholesterol in the media is shown

1150   as a percentage of the total cellular radioactivity (mean±SD). (C) Schematic of post-

1151   squaline cholesterol biosynthesis pathway with the sterols quantified by GC-MS

1152   named. Solid arrows indicate biosynthetic steps catalysed by EBP, SC5D and

1153   DHCR7. (D) Bar graph of sterols profile in wild-type and RAB18-null HeLa cells.

1154   Cells were grown in media supplemented with LPDS for 48 hours. Extracted sterols

1155   were analysed by gas chromatography-mass spectrometry (GC-MS). % Sterol was

1156   calculated as a proportion of total quantified sterols, excluding cholesterol, following

1157   normalization to a 5α-cholestane internal standard. n=3; ±s.e.m. (E) Positional root

1158   mean square fluctuations (RSMFs) for amino acid residues in simulations of ORP2-

1159   ORD complexed with cholesterol and lathosterol. Box and arrow show position of

1160   Tyr52 (Tyr110 in NP_653081). Simulations used a structure of the ORP2-ORD

1161   based on PDB 5ZM8. Parameters for lathosterol substituted the cholesterol double

1162   bond between C5-C6 with one between C7-C8. Simulations were performed with the

1163   CHARMM36 force field. (F) Still images from molecular dynamics simulations of the

1164   ORP2-ORD complexed with cholesterol (left) and lathosterol (right). Position of

1165   ORP2 Tyr110 and sterol-proximal water molecules are shown. (G) Plot to show the

1166   distance between Tyr52 and sterol 3' hydroxyl groups over time in each simulation.

1167   (H) Bar graphs to show incorporation of [^{3}H]-mevalonate and [^{3}H]-acetate into

1168   cholesterol in a panel of HeLa cell lines. Cells were grown in media supplemented

1169   with LPDS for 24 hours, then incubated with 5μCi/well [^{3}H]-mevalonate or 10μCi/well

1170   [^{3}H]-acetate for 24 hours. TLC was used to separate free cholesterol and

1171   radioactivity was quantified by scintillation counting (n=4; mean±SD). *$p<0.01$,

1172   **$p<0.001$, †$p<0.0005$.
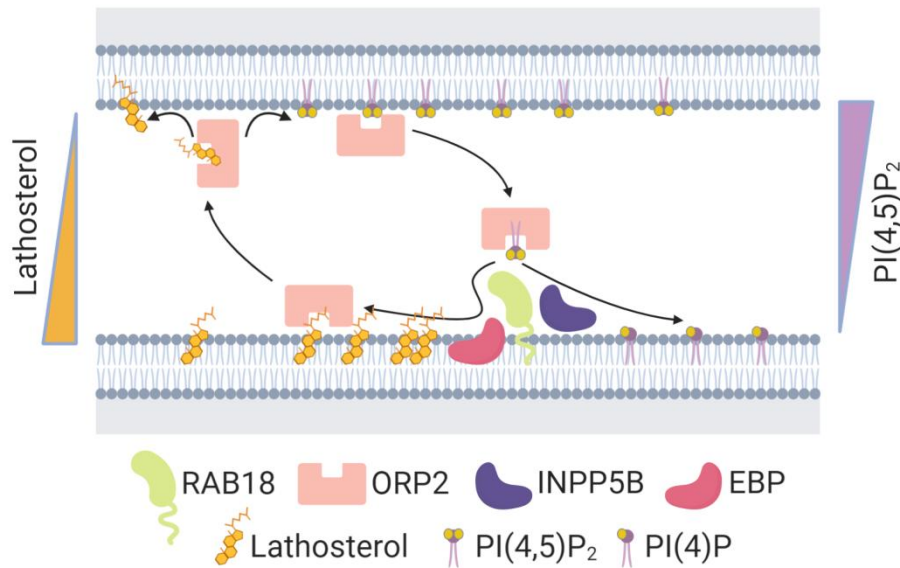
Figure 6. Model for lathosterol mobilization mediated by RAB18. ORP2 binds PI(4,5)P2 on an apposed membrane. RAB18 interacts with ORP2 and INPP5B promoting the hydrolysis of PI(4,5)P2 to PI(4)P and maintaining a PI(4,5)P2 concentration gradient. RAB18 then coordinates the biosynthesis of lathosterol by EBP and subsequent lathosterol mobilization by ORP2.